

FOR PEER REVIEW - CONFIDENTIAL

***C. elegans* neurons have functional dendritic spines**

Tracking no: 24-04-2019-TR-eLife-47918R1

Impact statement: *Caenorhabditis elegans* has *bona fide* dendritic spines, suggesting that the advantages of small model organisms, (1) genetic manipulations and (2) live-cell imaging, can be exploited to study dendritic spines.

Competing interests: No competing interests declared

Author contributions:

David Miller III: Conceptualization; Supervision; Funding acquisition; Project administration; Writing—review and editing

Funding:

HHS | NIH | National Institute of Neurological Disorders and Stroke (NINDS): David M Miller III, R01NS081259; HHS | NIH | National Institute of Neurological Disorders and Stroke (NINDS): David M Miller III, R01NS106951; American Heart Association (AHA): Andrea Cuentas-Condori, 18PRE33960581; National Science Foundation (NSF): Sierra Palumbos, DGE:1445197; Gouvernement du Canada | Canadian Institutes of Health Research (CIHR): Mei Zhen, FS154274; American Heart Association (AHA): Sierra Palumbos, 19PRE34380582 The funders had no role in study design, data collection and interpretation, or the decision to submit the work for publication.

Data Availability:

All data generated or analysed during this study are included in the manuscript and supporting files. Source data files have been provided for Figures 1, 4 and 5.

N/A

Ethics:

Human Subjects: No Animal Subjects: No

Information for reviewers (full submissions):

eLife aims to publish work of the highest scientific standards and importance in all areas of the life and biomedical sciences, from the most basic and theoretical work through to translational, applied and clinical research. Articles must be methodologically and scientifically rigorous, ethically conducted, and objectively presented according to the appropriate community standards.

You will be asked for a general assessment and a summary of any major concerns (ideally in fewer than 500 words), as well as a list of any minor comments (optional). You will also have the opportunity to comment on the statistical rigour of the work (optional).

In your general assessment, please articulate what is exciting and whether the work represents a significant contribution. Please note our guidelines about requests for additional work:

1. We will only request new work, such as experiments, analyses, or data collection, if the new data are essential to support the major conclusions. The authors must be able to do any new work in a reasonable time frame (additional work should be conducted and written up within two months); otherwise, we will usually reject the manuscript.
2. Any requests for new work must fall within the scope of the current submission and the technical expertise of the authors.

Our goal is to make peer review constructive and collaborative: after the reviews have been submitted independently, there is an online discussion between the reviewers in which each reviewer will see the identity of the other reviewers.

1
2
3
4
5
6
7
8
9
10
11
12

***C. elegans* neurons have functional dendritic spines**

Andrea Cuentas-Condori¹, Ben Mulcahy³, Siwei He², Sierra Palumbos², Mei Zhen³, *David M. Miller, III^{1,2}

Affiliations

1. Department of Cell and Developmental Biology, Vanderbilt University, Nashville, Tennessee, 37212, USA.

2. Neuroscience Program, Vanderbilt University, Nashville, Tennessee, 37212, USA.

3. Lunenfeld-Tanenbaum Research Institute, University of Toronto, Toronto, Ontario, M5G 1X5, Canada.

*Corresponding author: david.miller@vanderbilt.edu

13 **SUMMARY**

14 Dendritic spines are specialized postsynaptic structures that transduce presynaptic signals, are
15 regulated by neural activity and correlated with learning and memory. Most studies of spine
16 function have focused on the mammalian nervous system. However, spine-like protrusions have
17 been reported in *C. elegans* (Philbrook et al. 2018), suggesting that the experimental
18 advantages of smaller model organisms could be exploited to study the biology of dendritic
19 spines. Here, we used super-resolution microscopy, electron microscopy, live-cell imaging and
20 genetics to show that *C. elegans* motor neurons have functional dendritic spines that: (1) are
21 structurally defined by a dynamic actin cytoskeleton; (2) appose presynaptic dense projections;
22 (3) localize ER and ribosomes; (4) display calcium transients triggered by presynaptic activity
23 and propagated by internal Ca^{++} stores; (5) respond to activity-dependent signals that regulate
24 spine density. These studies provide a solid foundation for a new experimental paradigm that
25 exploits the power of *C. elegans* genetics and live-cell imaging for fundamental studies of
26 dendritic spine morphogenesis and function.

27

28 **KEY WORDS**

29 Dendritic spines, motor neuron, acetylcholine, *C. elegans*

30

31 **INTRODUCTION**

32 The majority of excitatory synapses in the mammalian brain feature short, local protrusions from
33 postsynaptic dendrites that respond to presynaptic neurotransmitter release (Rochefort and
34 Konnerth 2012). These dendritic “spines” were originally described by Ramon y Cajal (Yuste
35 2015) and are now recognized as key functional components of neural circuits. For example,
36 spine morphology and density are regulated by neural activity in plastic responses that are
37 strongly correlated with learning and memory (Kozorovitskiy et al. 2005; May-Britt et al. 1998).
38 Although spine-like protrusions have been reported for invertebrate neurons (Leiss et al. 2008;

39 Petralia et al. 2016), few studies (Bushey, Tononi, and Cirelli 2011; Scott, Reuter, and Luo
40 2003) have rigorously determined if these structures share functional features with vertebrate
41 spines.

42

43 The anatomy of the *C. elegans* nervous system was originally defined by reconstruction of
44 electron micrographs (EM) of serial sections. This approach revealed that a small subset of
45 neurons displays short, spine-like protrusions. These include five classes of motor neurons
46 (RMD, RME, SMD, DD, VD) and an interneuron (RIP) (White et al. 1976, 1986). Light and
47 electron microscopy detected similar dendritic protrusions extending from motor neurons in the
48 nematode, *Ascaris* (Angstadt, Donmoyer, and Stretton 1989; Stretton et al. 1978). Finally,
49 recent reports used light microscopy to show that a postsynaptic acetylcholine receptor is
50 localized near the tips of spine-like protrusions on the DD class motor neurons that directly
51 appose presynaptic termini (Oliver, Alexander, and Francis 2018; Philbrook et al. 2018). Here,
52 we have adopted a systematic approach to demonstrate that spine-like structures in GABAergic
53 motor neurons (DD and VD) exhibit the salient hallmarks of dendritic spines.

54

55 **RESULTS AND DISCUSSION**

56 **Dendritic spines in *C. elegans* GABAergic neurons**

57 In the adult, Dorsal D (DD) class GABAergic motor neurons extend axons to innervate dorsal
58 muscles and receive cholinergic input at ventral dendrites (Figure 1A). We used Airyscan
59 imaging, a type of super-resolution microscopy (Korobchevskaya et al. 2017), to detect spine-
60 like projections on the ventral processes of adult DD neurons labeled with a cytosolic mCherry
61 marker (Figure 1B). Because the actin cytoskeleton is a structural hallmark of vertebrate
62 dendritic spines (Cingolani and Goda 2008), we also labeled DD neurons with the actin marker,
63 LifeAct::GFP (Riedl et al. 2008). Super-resolution images detected apparent enrichment of
64 LifeAct::GFP in DD spines versus the dendritic shaft. For a quantitative assessment, we

65 calculated the ratio of the spine to shaft fluorescence (Figure 1D) and plotted the cumulative
66 distribution for each marker (Figure 1E). This representation shows a clear separation between
67 measurements of cytosolic mCherry that is evenly distributed throughout dendrites (median
68 spine/shaft ratio < 1) versus that of the LifeAct::GFP signal (median spine/shaft ratio > 1) (KS
69 test, $p < 0.0001$, Figure 1E). Thus, actin is enriched in DD spines. This interpretation is
70 strengthened by our finding that independent measurements of the spine density (mean spine
71 numbers/10 μm) with either cytoplasmic mCherry, LifeAct::GFP or the membrane bound
72 marker, myristolated-mRuby (myr::mRuby) are not significantly different (Figures 1F and S1A).
73 Similar results were obtained by EM reconstruction (see below) (Figure S1A).

74

75 A close inspection of LifeAct::GFP-labeled protrusions revealed a variety of spine shapes which
76 we grouped into morphological classes resembling those previously reported for mammalian
77 dendritic spines (Bourne and Harris 2008; Rochefort and Konnerth 2012): thin/mushroom,
78 filopodial, stubby and branched (Figure 1G-I) (see Methods). We merged “thin” and “mushroom”
79 shapes into a single category because both are defined by an enlarged head region vs a
80 narrower neck. By these criteria, adult DD neurons have predominantly thin/mushroom spines,
81 with lesser fractions of filopodial, stubby and branched shapes (Figure 1G and S1B-D). A
82 comparison of the morphological classes identified with the LifeAct::GFP vs MYR::mRuby
83 markers revealed some differences, notably the frequency of stubby spines, which is
84 significantly elevated with the MYR::mRuby label (Figure S1D). These differences could reflect
85 the relative ease of scoring different spine morphologies with markers for either the cell
86 membrane (myr::mRuby) or actin cytoskeleton (LifeAct::GFP). Alternatively, over-expression of
87 these markers could alter spine morphology but, in this case, does not appear to perturb overall
88 spine density (Figure S1A).

89

90 As an independent method for assessing the presence of dendritic spines, we used EM to
91 reconstruct the anterior-most 25 μm of the dendrite for DD1, the most anterior member of the
92 DD class of motor neurons (White et al. 1986). For this experiment, young adult animals were
93 prepared using High Pressure Freezing (HPF) to avoid potential artifacts arising from chemical
94 fixation (Mulcahy et al. 2018; Weimer et al. 2006; White et al. 1986). Reconstruction of 50 nm
95 serial ultrathin sections from the anterior DD1 dendrite detected twelve DD1 spines, with
96 multiple morphological shapes (Figure 2C) that resemble classes revealed by fluorescent
97 markers (Figure 1I; Figure S1B-C). EM reconstruction of mammalian dendritic spines in the
98 hippocampus also revealed that thin and mushroom shapes predominate (K M Harris and
99 Stevens 1989; Kristen M. Harris, Jensen, and Tsao 1992) and that filopodial and stubby spines
100 are less abundant (Fiala et al. 1998; Zuo et al. 2005).

101

102 **DD spines are shaped by a dynamic actin cytoskeleton**

103 Although we have assigned DD motor neuron spines to four discrete classifications, both
104 fluorescence imaging and EM reconstruction point to a broader array of spine types that
105 includes potential intermediate forms (Figure 1G-H; 2C). A similarly heterogeneous array of
106 spine shapes among mammalian neurons has been attributed to active remodeling of spine
107 architecture (Sala and Segal 2014; Zuo et al. 2005). To test for this possibility in *C. elegans*, we
108 used live imaging to produce time-lapse recordings of DD spines. Our live-imaging revealed
109 that some DD spines can remodel *in vivo* (Video 1). For example, Figure 1J depicts the
110 emergence of a LifeAct::GFP-labeled nascent lateral branch near the tip of a thin/mushroom
111 spine. During imaging sessions of ≥ 30 minutes, we observed cases of transient filopodial-like
112 extensions (11 out of 25 movies) from the dendritic shaft that retract in the course of minutes
113 (Videos 2-3). In contrast, most DD spines were stable throughout a given imaging session. In
114 the mature mammalian cortex, extended imaging has revealed transient filopodial extensions

115 with a lifetime shorter than a day, and potential plasticity over longer intervals, where
116 approximately half of spines are stable for months (Trachtenberg et al. 2002; Zuo et al. 2005).
117 To our knowledge, our time lapse images are the first to visualize dynamic dendritic spines in a
118 motor neuron of a living organism (Kanjhan, Noakes, and Bellingham 2016).

119

120 Live-imaging of DD motor neurons also detected a dynamic actin cytoskeleton (Figure S2A-E
121 and Videos 2-3), consistent with previous reports for mammalian dendritic spines (Honkura et
122 al. 2008; Mikhaylova et al. 2018). To ask if actin assembly is required for DD spine
123 morphogenesis (Cingolani and Goda 2008), we applied genetic methods to knock down key
124 regulators of actin polymerization and assessed their effect on DD spines (Figure S2F). We
125 found that the Arp2/3 complex, and two of its activators, the F-BAR protein TOCA-1 (Ho et al.
126 2004) and the Wave Regulatory Complex (Chen et al. 2010), are required to maintain DD spine
127 density (Figure S2F). Restoring expression of TOCA-1 to DD neurons rescued the spine density
128 defect (Figure S2G), demonstrating that actin polymerization is required cell-autonomously to
129 promote spine formation. Disruption of the Arp2/3 complex or its activators has been previously
130 shown to reduce dendritic spine density in the mammalian brain and to impair function (Kim et
131 al. 2013; Lippi et al. 2011; Soderling et al. 2003; Spence et al. 2016; Westphal et al. 2000).

132

133 **Dendritic spines of DD neurons directly appose presynaptic terminals**

134 Because functional dendritic spines are sites of presynaptic input (Alvarez and Sabatini 2007;
135 Hering, Sheng, and Medical 2001; Petralia et al. 2016), we investigated the disposition of DD
136 spines vis-a-vis their main presynaptic partners, the cholinergic VA and VB class motor neurons
137 (Figure 2A). For super-resolution imaging, we used the synaptic vesicle-associated marker,
138 mCherry::RAB-3, to label VA and VB presynaptic termini and LifeAct::GFP to label DD neurites
139 and spines (Figure 2B). Clusters of mCherry::RAB-3-labeled puncta are located adjacent to DD
140 spines (Figure 2B) (Philbrook et al. 2018). Among the 128 spines identified by LifeAct::GFP,

141 most (~84 %) reside near at least one presynaptic cluster (denoted “contacted” in Figure 2D).
142 Approximately ~40% (51/128) of DD spines are associated with multiple presynaptic clusters of
143 RAB-3 puncta which suggests that individual spines receive input from > 1 presynaptic terminal
144 (arrowheads, Figure 2B).

145

146 Our EM reconstruction of a segment of DD1 dendrite revealed 12 spines, all in direct apposition
147 with the presynaptic termini of cholinergic motor neurons (VA1, VA2 and VB2) (Figure 2C-D).
148 Of the 33 cholinergic presynaptic inputs in this region, 84.8% (n = 28/33) appose DD1 spines,
149 whereas only 15.2% (n = 5/33) are positioned along the dendritic shaft. This finding parallels the
150 observation that only 10% of excitatory synapses in the mature mammalian cortex are
151 positioned on dendritic processes (Cingolani and Goda 2008). Two thirds of DD1 spines (n =
152 8/12) receive input from more than one neuron class. That is, a single DD1 spine head is
153 contacted by presynaptic termini of both VA and VB class cholinergic motor neurons (Figure 2C
154 and Video 4). This finding could explain the observation above from Airyscan imaging that
155 multiple mCherry::RAB-3 puncta are adjacent to ~40% of DD spines (Figure 2B, arrowheads).
156 We note that individual spines on GABAergic neurons in the mammalian hippocampus can also
157 have inputs from multiple presynaptic termini (Acsady et al. 1998; Gulyás et al. 1992; Petralia et
158 al. 2016). Interestingly, the DD1 dendrite also receives a few inhibitory inputs from the other
159 class of GABAergic motor neurons (VD1), but most are restricted to the DD1 dendritic shaft (n =
160 5/6) (Figure 2C).

161

162 The acetylcholine receptor (AChR) subunit ACR-12 is postsynaptic to cholinergic inputs at
163 GABAergic motor neurons (Petrasch et al. 2013), and has been previously shown to localize to
164 DD1 dendritic protrusions (Figure 2E) (He et al. 2015; Philbrook et al. 2018). We used Airyscan
165 imaging to quantify the subcellular distribution of the ACR-12::GFP signal on DD spines. We
166 detected ACR-12::GFP clusters on ~95% of DD spines (n = 121/127) (Figure 2F-G), with 68.5%

167 (n = 87/127) localized at spine tips and the remainder either positioned along the lateral side of
168 the spine (~12%, n = 15/127) or at both the side and tip (~15 %, n = 19/127) (Figure 2G). 43.3%
169 of spines (n = 55/127) had more than one ACR-12::GFP cluster (Figure 2H), a finding that
170 mirrors a recent observation that spines of mammalian cortical neurons can display multiple
171 assemblages of the postsynaptic protein PSD-95 (Hruska et al. 2018).

172

173 To obviate the possibility that localization of ACR-12::GFP clusters to DD spines results from
174 over-expression, we used a new live-cell labeling scheme to detect an endogenous component
175 of the acetylcholine receptor complex, the co-factor protein LEV-10 (Gally et al. 2004). NATF
176 (Native and Tissue-Specific Fluorescence) relies on the reconstitution of superfolder GFP
177 (sfGFP) from the split-sfGFP fragments, GFP1-10 and GFP11 (He, Cuentas-Condori, and Miller
178 2019). We used genome editing to fuse seven tandem copies of GFP11 to the C-terminus of the
179 native LEV-10 coding sequence. When GFP1-10 was selectively expressed in DD neurons from
180 a transgenic array (i.e., *Pflp-13::GFP1-10*), we detected LEV-10 NATF-GFP signal at 100% (n =
181 159/159) of DD spines (Figure 2I-K), further substantiating the idea that DD spines are sites of
182 presynaptic input.

183

184 Our EM analysis confirmed that DD spines do not display electron dense postsynaptic densities
185 (PSDs), a feature that is also not detected in electron micrographs of most *C. elegans*
186 postsynaptic terminals (Lim et al. 2016; White et al. 1976, 1986; Zhen et al. 2000). Although
187 robustly stained PSDs are observed at vertebrate glutamatergic synapses, PSDs are either
188 absent or much less prominent in electron micrographs of vertebrate synapses at spines for
189 other neurotransmitters (glycine, GABA, acetylcholine) (Knott et al. 2002; Kubota et al. 2007;
190 Umbriaco et al. 1994). Postsynaptic assemblages at these synapses likely comprise distinct
191 sets of scaffolding proteins, some of which are readily stained by heavy atoms used for EM
192 imaging of glutamatergic synapses (Petralia et al. 2005, 2016).

193

194 **ER and ribosomes localize to DD neuron dendritic spines**

195 Key cytoplasmic organelles such as Smooth Endoplasmic Reticulum (SER), are present in both
196 dendritic shafts and spines of mammalian neurons (K M Harris and Stevens 1989). In addition
197 to its role of processing membrane proteins, spine SER regulates activity-dependent Ca^{++}
198 release through the ryanodine receptor (Fill and Copello 2002). Other structures such as
199 polysomes and rough ER have also been reported in spines, consistent with the possibility of
200 local translation at synapses (Bourne and Harris 2008; Hafner et al. 2019; Nimchinsky, Sabatini,
201 and Svoboda 2002; Steward, Reeves, and Reeves 1988).

202

203 Our EM reconstruction of DD1 revealed cisternae SER-like structures in both the dendritic shaft
204 and spines of DD1 (Figure 3A-B) and apparent ribosomes in some DD1 spines (Figure 3B'').

205 Consistent with this observation are our light microscopy images that detect the ribosomal
206 protein RPS-18::GFP (Noma et al. 2017) in about half of ($44.5 \pm 12.0\%$) DD spines (Figure 3C).

207 Mitochondria and microtubules are reported to be rare in the dendritic spines of mature
208 mammalian neurons (Bourne and Harris 2008; Nimchinsky, Sabatini, and Svoboda 2002). Our
209 EM reconstruction did not find mitochondria or microtubules in all twelve DD spines (Figure 3D),
210 while both organelles were detected in the DD1 dendritic shaft (Video 5). These observations
211 however should be interpreted cautiously given the small number of spines reconstructed.

212

213 **Activation of presynaptic cholinergic motor neurons drives Ca^{++} transients in DD spines**

214 Ca^{++} is a key signaling molecule to mediate activity-dependent synaptic plasticity (Lee et al.
215 2016; Rochefort and Konnerth 2012). We reasoned that functional DD spines should exhibit
216 dynamic Ca^{++} transients. To test this hypothesis, we expressed the Ca^{++} sensor GCaMP6s in
217 DD neurons. Live-imaging (at 2 second intervals) revealed spontaneous Ca^{++} transients in both
218 DD spines and shafts that lasted for several seconds (Figure 4A-C and Video 6). Muscle cells

219 that share cholinergic input with DD spines also display prolonged elevation of Ca^{++} over a
220 period of seconds (Liu, Chen, and Wang 2013), suggesting that cholinergic neurons regulate
221 the long lasting bursts of Ca^{++} in spines and muscle cells.

222

223 Interestingly, Ca^{++} transients were observed simultaneously in adjacent spines about 50% of the
224 time (Figure 4D). To estimate the likelihood of simultaneous Ca^{++} peaks occurring by chance,
225 we compared the distribution of the observed time differences between neighboring spine Ca^{++}
226 peaks (ΔT) to that of a uniform distribution (at 2 second intervals) over the period of observation
227 (20 seconds). These distributions are statistically different (KS test, $p < 0.0001$), suggesting that
228 Ca^{++} dynamics may reflect mechanisms for postsynaptic coordination of adjacent DD spine
229 activity (Figure 4D). Alternatively, coordinated Ca^{++} transients in adjacent spines could arise
230 from shared presynaptic neuron inputs. For example, the majority of DD1 spines (9/12) are
231 postsynaptic to the same cholinergic motor neuron VA2 (Figure 2C). A similar explanation of
232 convergent input was proposed for the coordinated firing of adjacent dendritic spines in rat
233 hippocampal neurons (Takahashi et al. 2012).

234

235 We did not observe Ca^{++} signals in DD spines when cholinergic receptors were desensitized by
236 administration of an agonist levamisole (data not shown). This finding is consistent with the
237 hypothesis that Ca^{++} transients in DD spines depend on presynaptic cholinergic signaling. To
238 test this idea, we engineered a transgenic animal for optogenetic activation of VA neurons with
239 ceChrimson (*Punc-4::ceChrimson::SL2::3xNLS::GFP*) (Schild and Glauser 2015) and detection
240 of Ca^{++} changes in DD spines with GCaMP6 (*Pflp-13::GCaMP6s::SL2::mCherry*). VA motor
241 neurons are presynaptic to DDs and therefore are predicted to evoke DD neuronal activity
242 (Philbrook et al. 2018; White et al. 1986). ceChrimson was activated by a brief flash of 561 nm
243 light (80ms) at 2.5 second intervals and the GCaMP6s signal in DD neurons was recorded at
244 2Hz. This experiment detected a correlation of GCaMP6s fluorescence with ceChrimson

245 activation (Figure 4E-G and Videos 7-8). Although GCaMP6s fluorescence also varied in DD
246 spines in the absence of 561 nm illumination, fluctuations were strongly correlated with
247 ceChrimson activation as shown by a plot of the standard deviation of GCaMP6s fluorescence
248 for all traces across the 15-second sampling period (Figure 4H). These results are consistent
249 with the interpretation that DD spines are responding to cholinergic input from presynaptic VA
250 motor neurons and parallel an earlier observation that DD dendritic protrusions are required for
251 cholinergic activation of Ca^{++} transients in DD cell soma (Philbrook et al. 2018).

252

253 Activation of ceChrimson triggered Ca^{++} changes at neighboring spines and in the DD shaft
254 (Figure 4F). As noted above, this effect could arise from shared input to adjacent spines from a
255 single presynaptic motor neuron (Figure 2C). Ca^{++} waves might also spread along the DD
256 dendrite from a locally activated spine. To test for this possibility, we restricted ceChrimson
257 activation to regions adjacent to single DD spines and recorded Ca^{++} changes (1) at the excited
258 spine; (2) at an adjacent spine and (3) at a distant spine (See Methods) (Figure 4I). Live
259 imaging two seconds after ceChrimson activation detected elevated GCaMP signals in spines in
260 all three regions that then waned with time (Figure 4J and Video 9). This observation suggests
261 that local cholinergic release can trigger Ca^{++} changes in neighboring and distant spines. In
262 developing hippocampal neurons, an initial Ca^{++} transient can be propagated to neighboring
263 spines via Ca^{++} release from intracellular stores (Lee et al., 2016). Because activation of
264 intracellular Ca^{++} stores depends on ryanodine-sensitive channels, we repeated the local spine
265 activation experiment (Figure 4I) in the presence of 1mM ryanodine. Blocking ryanodine
266 receptor-dependent Ca^{++} release substantially attenuated Ca^{++} transients in all spines (Figure
267 4K) thus suggesting that intracellular Ca^{++} is required to propagate the initial activation. In
268 hippocampal neurons, local glutamate uncaging triggers ryanodine-insensitive Ca^{++} transients in
269 the excited spine but this effect is rapid (~250 ms) (Lee et al. 2016) and thus a similar rapid
270 initial Ca^{++} transient might have been missed by our experimental set up that detects GCaMP

271 signals ~2 seconds after ceChrimson activation (Figure 4K). Our finding of prominent SER-like
272 structures in the DD shaft and spines is consistent with the idea that Ca⁺⁺ release from
273 intracellular stores could drive coordinated activation of adjacent spines (Figure 3A-B). Further,
274 a mutation that disrupts the UNC-68/Ryanodine receptor function results in substantially
275 reduced intrinsic Ca⁺⁺ dynamics in DD spines (Figure S3A). Together, our results suggest that
276 Ca⁺⁺ signals can propagate to nearby spines after local activation and that spreading depends
277 on intracellular Ca⁺⁺ stores.

278

279 **Cholinergic signaling enhances DD spine density during development.**

280 In mammalian neurons, spine shape and density are modulated throughout development (Fiala
281 et al. 1998; Kristen M. Harris, Jensen, and Tsao 1992; Kanjhan et al. 2016). LifeAct::GFP
282 imaging in late larval to adult stages (L3, early L4, mid-L4 and young adult), revealed that spine
283 density increases as DD neurons elongate during development (Figures 5B, 5E and S4A).

284

285 Dendritic spines can be modulated by changes in synaptic strength (Bourne and Harris 2008;
286 Nimchinsky, Sabatini, and Svoboda 2002; Rochefort and Konnerth 2012). Long-term
287 potentiation is correlated with increased numbers of spines in the mammalian brain (Engert and
288 Bonhoeffer 1999; Trachtenberg et al. 2002, 2005). Similarly, hyperactivity is associated with
289 increased dendritic spine density in hypoglossal motor neurons (Kanjhan, Noakes, and
290 Bellingham 2016). Conversely, long-term depression induces spine shrinkage (Zhou, Homma,
291 and Poo 2004) and may lead to their elimination (Hasegawa et al. 2015).

292

293 We tested whether DD spines respond to changes in cholinergic input by altering acetylcholine
294 levels. To reduce cholinergic signaling, we used *unc-17/vAChT (e113)* mutants, in which
295 expression of the vesicular acetylcholine transporter vAChT is selectively eliminated in ventral
296 cord cholinergic motor neurons (J. Rand, personal communication). Conversely, to elevate

297 cholinergic signaling, we used *ace-1(p100);ace-2(g720)* mutants that disrupt
298 acetylcholinesterase activity (Figure 5A). Reduced acetylcholine release in the *unc-17/vAChT*
299 mutant results in reduced DD spine density at the L4 larval stage (Figure 5C, 5E and S4B). In
300 contrast, increased acetylcholine levels (i.e., in *ace-1;ace-2* mutants) results in precocious
301 elevation of spine density during development (Figure 5D, 5E and S4C). Importantly, either
302 chronic reduction (i.e., in the *unc-17/vAChT* mutant) or elevation (i.e., in *ace-1;ace-2* double
303 mutants) of acetylcholine levels (Figure S4B and S4C) impaired the developmentally regulated
304 enhancement of spine density that is normally observed in wild-type animals. These findings are
305 consistent with the idea that cholinergic signaling positively regulates the formation of DD
306 spines. The developmental elevation of spine density is also blocked in *unc-31/CAPS* mutants
307 (Speese et al. 2007), in which neuropeptide and catecholamine neurotransmitter release is also
308 prevented (Figure S4D and S4E).

309

310 For an additional test of activity-dependent regulation of DD spine density, we modulated
311 presynaptic cholinergic function for specific periods during larval development. To reduce
312 cholinergic activity, we expressed the histamine-gated chloride channel (Pokala et al. 2014) in
313 A-class (DA, VA) cholinergic motor neurons, presynaptic partners of DD neurons (Figure 2C)
314 (White et al. 1976). Animals grown in the presence of histamine showed reduced spine density
315 at the L4 stage compared to animals grown on plates without histamine (Figure 5F-I). To
316 elevate cholinergic activity, we expressed ceChrimson (Schild and Glauser 2015) in A-class
317 motor neurons and measured spine density at the L3 stage when wild-type animals show fewer
318 DD spines than in adults (Figure 5B and 5E). Animals were exposed to 561 nm light to activate
319 ceChrimson for a brief period (1 second every 4 seconds) during the L2-L3 stage larval
320 development (See Methods). This treatment led to increased spine density (scored in L3 larvae)
321 in comparison to animals without ceChrimson stimulation (Figure 5J-M). These results
322 demonstrate that DD spine density depends on presynaptic cholinergic signaling. Thus DD

323 spines share the property of mammalian dendritic spines of positive regulation by neuronal
324 activity (Kanjhan et al. 2016; Trachtenberg et al. 2005).

325

326 **VD-class GABAergic neurons also display dendritic spines.**

327 In the adult *C. elegans* motor circuit, dendrites of the DD-class GABAergic motor neurons
328 receive cholinergic input in the ventral nerve cord, whereas the VD class receives input in the
329 dorsal nerve cord (Figure S3A). Because the original EM reconstruction of the *C. elegans*
330 nervous system detected spine-like structures on VD neurons (White et al. 1976), we sought to
331 verify this finding by using the LifeAct::GFP marker for Airyscan imaging. We used miniSOG (Qi
332 et al. 2012) for selective ablation of DDs (See Methods) since the LifeAct::GFP marker (*Punc-*
333 *25::LifeAct::GFP*), in this case, was expressed in both DD and VD neurons. This experiment
334 confirmed the presence of dendritic spines in VD neurons throughout the dorsal nerve cord
335 (Figure S5A-D).

336

337 Our EM reconstruction of 27 μm of the anterior VD2 dendrite detected 9 dendritic spines (Figure
338 S3E). Similar to DD1, most VD spines are juxtaposed to presynaptic termini of cholinergic motor
339 neurons (DA2, DB1, AS2). Additional presynaptic inputs from other cholinergic and GABAergic
340 motor neurons (DD1) are distributed along the dendritic shaft (Figure S3F). Several
341 mitochondria are also observed in VD2 dendritic shaft (Figure S3E). Thus, both the DD and VD
342 classes of ventral cord GABAergic motor neurons display dendritic spines (White et al. 1976,
343 1986).

344

345 **Why study dendritic spines in *C. elegans*?**

346 The prevalence of postsynaptic protrusions in vertebrate and invertebrate nervous systems
347 suggests that spines are ancient structures and thus could be effectively investigated in a
348 variety of model organisms (Leiss et al. 2008; Petralia et al. 2016). Our analyses revealed

349 salient, conserved features of *C. elegans* dendritic spines: (1) A key role for the actin
350 cytoskeleton in spine morphogenesis; (2) Postsynaptic receptor complexes at the tips of spines
351 in close proximity to presynaptic active zones; (3) Postsynaptic calcium transients evoked by
352 presynaptic activity and propagated from intracellular Ca⁺⁺ stores; (4) The presence of
353 endoplasmic reticulum and ribosomes; (5) Regulation of spine density by presynaptic activity.

354

355 *C. elegans* offers several advantages for studies of spine morphogenesis and function. Because
356 *C. elegans* is transparent, live imaging does not require surgery or other invasive methods that
357 are typically necessary for *in vivo* imaging of spines in an intact mammalian nervous system.
358 Well-developed *C. elegans* genetic tools for targeted genomic manipulation (Nance and
359 Frøkjær-Jensen 2019) and unbiased forward genetic screens can be used to reveal new
360 determinants of spine assembly. A recent study, for example, reported that neurexin, a
361 conserved membrane protein and established regulator of synaptic assembly, is necessary for
362 spine morphogenesis in DDs. Interestingly, in this case, neuroligin, the canonical neurexin
363 ligand, is not required, suggesting a potentially new neurexin-dependent mechanism of
364 synaptogenesis (Oliver, Alexander, and Francis 2018; Philbrook et al. 2018).

365

366 Our study confirmed that both DD and VD motor neurons display dendritic spines. Thus, other
367 neurons reported to have “short branches” in the original EM reconstruction of the adult *C.*
368 *elegans* (White et al. 1986), the cholinergic (RMD, SMD) and GABAergic (RME) motor neurons
369 and the interneuron (RIP), are likely to display *bona fide* dendritic spines. An ongoing effort to
370 produce a gene expression fingerprint of each type of *C. elegans* neuron (Hammarlund et al.
371 2018; Taylor et al. 2019) may be useful for identifying genetic programs that uniquely correlate
372 with spine morphogenesis since only a small number (White et al. 1976) of neurons have been
373 reported to have spine-like structures. Finally, a developmentally regulated remodeling program
374 (Kurup and Jin 2016; Petersen et al. 2011; John G. White, Albertson, and Anness 1978)

375 transforms presynaptic boutons into postsynaptic spines in larval DD neurons and thus could be
376 especially useful for live imaging studies of synaptic plasticity and spine morphogenesis.

377

378 **ACKNOWLEDGEMENTS**

379 We thank M. Francis and Alison Philbrook for sharing unpublished observations. We thank
380 Douglas Holmyard (Nanoscale Biomedical Imaging Facility) for preparing EM samples and
381 serial EM sections; Dylan Burnette, Aidan Fenix and Nilay Taneja for insightful imaging
382 discussions; and Erin Miller for help with aligning serial electron micrographs. Some *C. elegans*
383 strains used in this work were provided by the Caenorhabditis Genetics Center, which is funded
384 by the NIH Office of Research Infrastructure Programs (P40 OD010440). Airyscan and live-
385 imaging data was acquired at the Vanderbilt Cell Imaging Shared Resource (supported by NIH
386 grants CA68485, DK20593, DK58404, DK59637 and EY08126). This work was supported by
387 National Institutes of Health grants to DMM (R01NS081259 and R01NS106951), American
388 Heart Association predoctoral fellowships to ACC (18PRE33960581) and SP
389 (19PRE34380582), National Science Foundation GRFP to SP (DGE:1445197) and a Canadian
390 Institute of Health Research grant to MZ (FS154274).

391

392

393

394

395

396

397

398

399

400 **DECLARATION OF INTERESTS**

401 The authors declare no financial interests.

402

403 METHODS

404 Plasmids used in this study:

405

Plasmid Name	Description	Cloned by
pACC4	punc-25::LifeAct::GFP	Gateway cloning
pACC6	pflp-13::LifeAct::GFP	InFusion cloning
pACC12	pflp-13::LifeAct::mCherry	InFusion cloning
pACC22	pflp-13::toca-1a::mCherry	InFusion cloning
pACC83	pflp-13::GCaMP6s::SL2::mCherry	InFusion cloning
pACC86	punc-4::ceChrimson::SL2::mCherry	InFusion cloning
pACC92	punc-4::ceChrimson::SL2::3xNLS::GFP	InFusion cloning
pMLH09	punc-25::gateway::GFP	Gift
pSH4	pmyo-2::RFP	Gift
pSH21	pstr-1::GFP	InFusion cloning
pSH40	punc-4::HisCl::SL2::mCherry	Gift
pSH83	pflp-13::miniSOG::SL2::BFP	InFusion cloning
pACC128	pflp-13::myr::mRuby3	InFusion cloning

406

407 Strains used in this study:

Strain Name	Description	Reference
XMN46	bgIs6 [pflp-13::mCherry; Ptx-3::RFP] II	(Opperman and Grill 2014)
NC3315	wdEx1016 [<i>pflp-13::LifeAct::GFP</i> ; <i>pmyo-2::RFP</i>]	This study
NC3376	ufls63 (<i>pacr-2::RAB3::mCherry</i>) ; wdEx1016[<i>pflp-13::LifeAct::GFP</i> ; <i>pmyo-2::RFP</i>]	This study
NC3458	<i>eri-1(mg366)</i> ; wdEx1016 [<i>pflp-13::LifeAct::GFP</i> ; <i>pmyo-2::RFP</i>]	This study
NC3355	<i>toca-1(tm2056)</i> X; wdEx1016 [<i>pflp13::LifeAct::GFP</i> ; <i>pmyo-2::RFP</i>]	This study
NC3357	wdEx1029 [<i>pflp13::LifeAct::GFP</i> ; <i>punc4::HisCl::SL2::mCherry</i> ; <i>pmyo-2::RFP</i>]	This study

NC3455	<i>ace-2(g72) I ; ace-1(p100) X; wdEx1016 [pflp-13::LifeAct::GFP; pmyo-2::RFP]</i>	This study
NC3462	<i>unc-17(e113) IV; wdEx1016 [pflp-13::LifeAct::GFP; pmyo-2::RFP]</i>	This study
NC3469	<i>wdEx1069 [pflp13::LifeAct::mCherry; pstr-1::GFP]</i>	This study
NC3480	<i>wdEx1074 [pflp-13::miniSOG::SL2::BFP; punc-25::LifeActGFP; pmyo-2::RFP]</i>	This study
NC3482	<i>acr-12(ok367) ufls126 [pflp-13::ACR12::GFP] X, wdEx1069 [pflp-13::LifeActmCherry; pstr-1::GFP]</i>	This study
NC3484	<i>wdEx1078 [pflp-13::GCaMP6s::SL2::mCherry; pmyo-2::RFP]</i>	This study
NC3486	<i>unc-31(e169) IV; wdEx1016 [pflp-13::LifeAct::GFP; pmyo-2::RFP]</i>	This study
NC3489	<i>wdEx1083 [punc-4::ceChrimson::SL2::mCherry; pflp-13::LifeAct::GFP; pmyo-2::RFP]</i>	This study
NC3569	<i>lin-15(n765); wdlS117 [punc-4::ceChrimson::SL2::3xNLSGFP; lin-15+] ; wdEx1112 [pflp13::GCaMP6s::SL2::mCherry]</i>	This study
NC3608	<i>wdEx123[pflp-13::myr::mRuby; pstr-1::GFP]</i>	This study
NC3609	<i>toca-1(tm2056); wdEx124[pflp-13::toca-1a::mCherry; pflp-13::LifeAct::GFP; pmyo-2::RFP]</i>	This study
NC3610	<i>unc-68(r1162) V; wdEx1112 [pflp13::GCaMP6s::SL2::mCherry]</i>	This study

408

409 Worm Breeding

410 Worms were maintained at 20°- 25°C using standard techniques(Brenner 1974). Strains were
411 maintained on NGM plates seeded with *E. coli* (OP-50) unless otherwise stated. The wild type
412 (WT) is N2 and only hermaphrodite worms were used for this study. Staging as L3, early L4

413 (eL4), L4 and young adult worms was defined following vulva development as previously
414 reported (Chia, Patel, and Shen 2012).

415 Molecular Biology

416 Gateway cloning was used to build pACC06 (*punc-25::LifeAct::GFP*). Briefly, plasmid
417 pDONR221 (Plastino Lab) (Havrylenko et al. 2015) was used in the LR reaction with pMLH09
418 (*punc-25::ccdB::GFP*) to create pACC06. Additional plasmids were created using InFusion
419 cloning (Takara). The InFusion cloning module (SnapGene) was used to design primers to
420 create the desired plasmid. Briefly, vector and insert fragments were amplified using CloneAmp
421 HiFi polymerase. PCR products were gel-purified and incubated with In-Fusion enzyme for
422 ligations. Constructs were transformed into Stellar Competent cells and confirmed by
423 sequencing (See full list of plasmids). Plasmids are available upon request. Addgene provided
424 sequences for GCamP6s (#68119), and *C. elegans*-optimized Chrimson (ceChrimson, #66101)
425 (Schild and Glauser 2015). miniSOG sequence was a gift from the Jin lab (Qi et al. 2012).
426 pSH40 was a gift from the Bargmann Lab (Pokala et al. 2014). *C. elegans*-optimized mRuby3
427 was a gift from Peri Kurshan (Shen Lab). TOCA-1a cDNA was a gift from Barth Grant (Bai and
428 Grant 2015).

429 Feeding RNAi

430 Clones from the RNAi feeding library (Source BioScience) were used in this study. RNAi plates
431 were produced as described (Petersen et al. 2011). Briefly, RNAi bacteria were grown in the
432 presence of ampicillin (50 µg/mL) and induced with IPTG (1 mM). 250µL of the RNAi bacterial
433 culture was seeded on NGM plates. RNAi plates were kept at 4°C for up to one week until used.
434 RNAi experiments were set-up as follows: 3 to 5 L4 worms (NC3458) were placed on RNAi
435 plates and maintained at 20°C. Four days later, F1 progeny was imaged as young adults.

436 Electron Microscopy

437 Young adult animals were fixed using high pressure freezing followed by freeze substitution, as
438 previously described (Mulcahy et al. 2018; Rostaing et al. 2004), with minor modification: they

439 were held at -90°C in acetone with 0.1% tannic acid and 0.5% glutaraldehyde for 4 days,
440 exchanged with 2% osmium tetroxide in acetone, raised to -20°C over 14h, held at -20°C for
441 14h, then raised to 4°C over 4h before washing. Additional *en bloc* staining was performed with
442 uranyl acetate for 2h at room temperature, followed by lead acetate at 60°C for 2h. Samples
443 were embedded in Epon, cured at 60°C for 24h, then cut into 50nm-thick serial sections.
444 Sections were not poststained. Images were taken on a FEI Tecnai 20 transmission electron
445 microscope with a Gatan Orius digital camera, at 1nm/pixel.

446 3D reconstruction

447 Images were aligned into a 3D volume and segmented using TrakEM2 (Cardona et al. 2012), a
448 Fiji plugin (Schindelin et al. 2012). Neuron identity was assigned based on characteristic
449 morphology, process placement, trajectory and connectivity (Mulcahy et al. 2018; White et al.
450 1986). The ventral and dorsal cord volumes contained the anterior-most 25 μm of DD1, and 27
451 μm of VD2, respectively. Volumetric reconstructions were exported to 3Ds Max for processing
452 (3Ds Max, Autodesk)

453 Airyscan Microscopy

454 Worms were mounted on 10% agarose pads and immobilized with 15mM levamisole/0.05%
455 tricaine dissolved in M9. A Zeiss LSM880 microscope equipped with an Airyscan detector and a
456 63X/1.40 Plan-Apochromat oil objective lens was used to acquire super resolution images of the
457 DD neuron. Images were acquired as a Z-stack (0.19 μm /step), spanning the total volume of the
458 DD ventral process and submitted for Airyscan image processing using ZEN software.
459 Developmental stage was determined by scoring gonad and vulva development (Schindler and
460 Sherwood 2013).

461 Classification of spines

462 Spine shapes were determined from Z-projections of Airyscan images and by 3D-EM
463 reconstruction. Mean and SD were determined using GraphPad. Spines were classified as
464 thin/mushroom, filopodial, stubby or branched. Thin/mushroom spines displayed a constricted

465 base (neck) and an expanded tip (head). Filopodial spines do not have a constricted base (no
466 neck) but are protrusions of constant width. Stubby spines were recognized as protrusions with
467 a wide base and tip. Branched spines were identified as protrusions with more than one visible
468 tip.

469 Ribosomal protein labeling in DD spines

470 To label ribosomes in DD spines, we used DD-specific RIBOS(Noma et al. 2017). To label DD
471 spines we injected *Pflp-13::LifeAct::mCherry* plasmid into CZ20132 and used Airyscan imaging
472 to examine transgenic animals (See Airyscan microscopy section).

473 Actin dynamics

474 A Nikon microscope equipped with a Yokogawa CSU-X1 spinning disk head, Andor DU-897
475 EMCCD camera, high-speed piezo stage motor, 100X/1.49 Apo TIRF oil objective lens and a
476 1.5X magnification lens was used for live imaging. For measurements of LifeAct::GFP and
477 cytosolic mCherry dynamics, L4 and young adults (NC3315 and XMN46) were mounted on 10%
478 agarose pads and immobilized with 15mM levamisole/0.05% tricaine dissolved in M9. Z-stacks
479 (0.5 μ m/step) were collected every 3 minutes. Movies were submitted to 3D-deconvolution on
480 NIS-Elements using the Automatic algorithm and aligned with the NIS Elements alignment tool.
481 For each movie, ROIs were defined along the dendritic shaft for each spine. Mean ROI Intensity
482 was calculated for each time point and exported to Microsoft Excel. Background was
483 determined from a neighboring region inside the worm and subtracted from the ROI in each
484 timepoint. Mean intensity changes were normalized to the mean Intensity from the first
485 timepoint of each movie. Intensity changes for LifeAct::GFP and mCherry were graphed using
486 Prism6 software.

487 GCaMP6s dynamics in DD spines.

488 GCaMP6s imaging was performed on a Nikon microscope equipped with a Yokogawa CSU-X1
489 spinning disk head, Andor DU-897 EMCCD camera, high-speed piezo, 100X/1.49 Apo TIRF oil
490 objective lens and a 1.5X magnification lens. NC3484 worms were immobilized using a

491 combination of 3 μ L of 100mM muscimol (TOCRIS biosciences #0289) and 7 μ L 0.05um
492 polybeads (2.5% solids w/v, Polysciences, Inc. #15913-10). Triggered acquisition was used to
493 excite the GCaMP and mCherry signals with 488nm and 561nm lasers. Single plane movies
494 were collected every second for at least 24 seconds. Movies were submitted for 2D-
495 deconvolution on NIS-Elements using the Automatic algorithm. Movies collected with NIS-
496 elements were aligned through time using the ND alignment tool. ROIs with the same area for
497 each channel were defined in spines and on a neighboring region to determine background
498 intensity for every time point. Mean ROI intensity was exported to Microsoft Excel for subtraction
499 of mean fluorescence background intensity. Fluorescence at each timepoint was normalized to
500 intensity at t=0 for GCaMP6s and mCherry signals. Local peaks of GCaMP6s fluorescence
501 were identified between neighboring neurons and the difference between the timepoints (ΔT)
502 was calculated. Traces were graphed on Prism6.

503 To detect evoked calcium responses in DD neurons, NC3569 was grown for 1 generation on an
504 OP50-seeded plate with freshly added ATR or carrier (EtOH). L4 worms were glued (Super
505 Glue, The Gorilla Glue Company) to a microscope slide in 2 μ L 0.05um polybeads (2.5% solids
506 w/v, Polysciences, Inc. #15913-10) plus 3 μ L of M9 buffer and imaged under a coverslip.

507 GCaMP6s dynamics were recorded after all-spines activation on a Nikon microscope equipped
508 with a Yokogawa CSU-X1 spinning disk head, Andor DU-897 EMCCD camera, high-speed
509 piezo and 100X/1.49 Apo TIRF oil objective lens. Single plane images encompassing DD1
510 postsynaptic spines and adjacent VA and DA motor neurons were collected at 2 frames/second
511 for 15 seconds. The sample was illuminated with a 561nm laser at 2.5 sec intervals (e.g., every
512 5 frames) for red light activation of ceChrimson expressed in cholinergic DA and VA motor
513 neurons (*Punc-4::ceChrimson::SL2::3xNLS::GFP*) while maintaining constant illumination with a
514 488nm laser to detect GCaMP6s signals.

515 We used a sequential excitation/imaging protocol to measure Ca⁺⁺ transients in spines after
516 local activation of cholinergic release. GCaMP6s signals were recorded after a single-spine

517 activation on a Nikon A1R laser scanning confocal microscope using a 60X/1.4 N.A oil objective
518 lens with Nyquist acquisition. A stimulation ROI was defined adjacent to a single DD1 or DD2
519 spine and illuminated with the 561nm laser for less than 200 ms. GCaMP6s changes were
520 recorded with 488nm laser every 2 seconds for 30 seconds and 561nm excitation was triggered
521 after the 4th imaging time-point. Ryanodine-treated worms were soaked in 1mM ryanodine
522 (TOCRIS biosciences #1329) for 15 minutes before the imaging session and mounted on a slide
523 using glue as above.

524 For quantifying GCaMP6s fluorescence, videos were aligned and 2D-deconvolved using NIS
525 Elements software. Three regions of interest were defined to evaluate average fluorescence
526 intensity from (1) a spine at the site of excitation; (2) an adjacent spine and (3) a distant spine,
527 i.e., at least 9 μm away from the excitation point. Signal was collected from separate ROIs
528 drawn on each spine and on a nearby region to capture background fluorescence. Mean
529 fluorescence intensity of each ROI was exported into Excel for analysis. Background
530 fluorescence was subtracted from each frame and measurements were normalized to the initial
531 time-point. Mean fluorescence traces were plotted using Prism6. Statistical analysis compared
532 average GCaMP6s intensity of the first 4 frames vs GCaMP6s after stimulation (5th frame) using
533 the Kruskal Wallis test for non-parametric samples and multiple comparisons.

534

535 Temporal neuronal silencing with histamine chloride

536 Gravid adults were allowed to lay eggs for 2 hours on an OP50-seeded plate at 20 C to produce
537 a synchronized population of L1 larvae. The middle time-point of the egg-laying session was
538 considered T_0 . At T_{19} (time in hours), L1 larvae were transferred to control or histamine plates
539 and maintained at 20°C until imaging on an LSM880 Airyscan microscope at the young adult
540 stage. For control plates, 200 μL of water was added to OP-50 seeded NGM plates. For
541 histamine plates, 200 μL of 0.5M Histamine, diluted in water, was added to OP-50 seeded NGM
542 plates.

543 Temporal neuronal activation

544 Gravid adults were allowed to lay eggs for 2 hours on an OP-50-seeded plate with freshly added
545 ATR. The resultant synchronized population of L1 larvae was maintained at room temperature
546 (23-25C). At T₂₇ (L2 larvae), we used WormLab (MBF Bioscience) for exposure to repetitive
547 cycles of 1 second ON + 4 seconds OFF for 6 hours of a 617nm precision LED (Mightex PLS-
548 0617-030-10-S). Images were collected on an LSM880 Airyscan microscope with 60X/1.4 Plan-
549 Apochromat oil objective lens. Control worms were not exposed to light but grown on ATR
550 plates. 100mM ATR (Sigma, #A7410) was prepared in ethanol and stored at -20C. 300uM of
551 ATR was added to OP-50 bacteria and seeded on NGM plates. Plates were dried in darkness
552 overnight and used the next day for experiments.

553 Image Analysis

554 FIJI (Schindelin et al. 2012) and NIS-Elements software were used for data quantification. Z-
555 stacks were flattened in a 2D projection and line scans were manually drawn along protrusions
556 and perpendicular to the proximal shaft (Figure 1d) to determine the Protrusion/Shaft ratio
557 (Figure 1e). Spine density was calculated using the counting tool in NIS Elements and then
558 normalized to number of spines per 10 µm of dendrite length.

559 Statistical Analysis

560 For comparison between 2 groups, Student's T-test was used and p<0.05 was considered
561 significant. ANOVA was used to compare between 3 or more groups followed by Dunnett's
562 multiple-comparison test. Standard Deviations between two samples were compared using an
563 F-test and considered p<0.05 as significant.

564 Ablation of DD neurons

565 Twenty gravid adults (NC3480) were allowed to lay eggs for 2 hours with the middle time point
566 considered T₀. At T₁₆, (hours) DD neurons were ablated by miniSOG(Qi et al. 2012) activation
567 by exposing worms for 45 min to a 470nm LED light (#M470L2, Thor Labs). Animals were then
568 maintained at 20°C until imaging at ~T₆₀ as young adults.

569

570 **REFERENCES**

571

572 Acsady, Laszlo et al. 1998. "GABAergic Cells Are the Major Postsynaptic Targets of Mossy

573 Fibers in the Rat Hippocampus." *The Journal of neuroscience* 18(9): 3386–3403.

574 Alvarez, Veronica A., and Bernardo L. Sabatini. 2007. "Anatomical and Physiological Plasticity

575 of Dendritic Spines." *Annual Review of Neuroscience* 30(1): 79–97.

576 <http://www.annualreviews.org/doi/10.1146/annurev.neuro.30.051606.094222>.

577 Angstadt, James D., Judith E. Donmoyer, and Antony O.W. Stretton. 1989. "Retrovesicular

578 Ganglion of the Nematode *Ascaris*." *Journal of Comparative Neurology* 284(3): 374–88.

579 Bai, Zhiyong, and Barth D Grant. 2015. "A TOCA/CDC-42/PAR/WAVE Functional Module

580 Required for Retrograde Endocytic Recycling." *Proceedings of the National Academy of*

581 *Sciences of the United States of America* 112(12): E1443-52.

582 [http://www.pubmedcentral.nih.gov/articlerender.fcgi?artid=4378436&tool=pmcentrez&rend](http://www.pubmedcentral.nih.gov/articlerender.fcgi?artid=4378436&tool=pmcentrez&rendertype=abstract)

583 [ertype=abstract](http://www.pubmedcentral.nih.gov/articlerender.fcgi?artid=4378436&tool=pmcentrez&rendertype=abstract).

584 Bourne, Jennifer N, and Kristen M Harris. 2008. "Balancing Structure and Function at

585 Hippocampal Dendritic Spines." *Annual Review of Neuroscience* 31(1): 47–67.

586 <http://www.annualreviews.org/doi/10.1146/annurev.neuro.31.060407.125646>.

587 Brenner, S. 1974. "The Genetics of *Caenorhabditis Elegans*." *Genetics* 77: 71–94.

588 Bushey, Daniel, Giulio Tononi, and Chiara Cirelli. 2011. "Sleep and Synaptic Homeostasis:

589 Structural Evidence in *Drosophila*." *Science* 332(June): 1576–82.

590 Cardona, Albert et al. 2012. "TrakEM2 Software for Neural Circuit Reconstruction." *PLoS ONE*

591 7(6).

592 Chen, Zhucheng et al. 2010. "Structure and Control of the Actin Regulatory WAVE Complex."

593 *Nature* 468. <http://www.nature.com.proxy.library.vanderbilt.edu/articles/nature09623.pdf>

594 (January 13, 2018).

595 Chia, Poh Hui, Maulik R Patel, and Kang Shen. 2012. "NAB-1 Instructs Synapse Assembly by

596 Linking Adhesion Molecules and F-Actin to Active Zone Proteins.” *Nature neuroscience*
597 15(2): 234–42.
598 <http://dx.doi.org/10.1038/nn.2991><http://www.ncbi.nlm.nih.gov/pubmed/22231427>.

599 Cingolani, Lorenzo a, and Yukiko Goda. 2008. “Actin in Action: The Interplay between the Actin
600 Cytoskeleton and Synaptic Efficacy.” *Nature Reviews Neuroscience* 9(5): 344–56.
601 <http://www.nature.com/doi/10.1038/nrn2373>.

602 Engert, Florian, and Tobias Bonhoeffer. 1999. “Dendritic Spine Changes Associated with
603 Hippocampal Long-Term Synaptic Plasticity.” *Nature* 399(May).

604 Fiala, John, Marcia Feinberg, Viktor Popov, and Kristen M. Harris. 1998. “Synaptogenesis via
605 Dendritic Filopodia in Developing Hippocampal Area CA1.” *The Journal of neuroscience*
606 18(21): 8900–8911.

607 Fill, M., and J. A. Copello. 2002. “Ryanodine Receptor Calcium Release Channels.”
608 *Physiological Reviews* 82(4): 893–922.
609 <http://physrev.physiology.org/cgi/doi/10.1152/physrev.00013.2002>.

610 Gally, C et al. 2004. “A Transmembrane Protein Required for Acetylcholine Receptor Clustering
611 in *C. Elegans*.” *Nature* 431(September).
612 <http://www.wormbase.org/db/misc/paper?name=WBPaper00024805>.

613 Gulyás, A. I., R. Miettinen, D. M. Jacobowitz, and T. F. Freund. 1992. “Calretinin Is Present in
614 Non-Pyramidal Cells of the Rat Hippocampus-I. A New Type of Neuron Specifically
615 Associated with the Mossy Fibre System.” *Neuroscience* 48(1): 1–27.

616 Hafner, Anne Sophie et al. 2019. “Local Protein Synthesis Is a Ubiquitous Feature of Neuronal
617 Pre- And Postsynaptic Compartments.” *Science* 364(6441).

618 Hammarlund, Marc, Oliver Hobert, David M. Miller, and Nenad Sestan. 2018. “The CeNGEN
619 Project: The Complete Gene Expression Map of an Entire Nervous System.” *Neuron* 99(3):
620 430–33. <https://doi.org/10.1016/j.neuron.2018.07.042>.

621 Harris, K M, and John K Stevens. 1989. “Dendritic Spines of CA 1 Pyramidal Cells in the Rat

622 Hippocampus: Serial Electron Microscopy with Reference to Their Biophysical
623 Characteristics.” *The Journal of neuroscience : the official journal of the Society for*
624 *Neuroscience* 9(8): 2982–97.

625 Harris, Kristen M., Frances Jensen, and Beatrice Tsao. 1992. “Three-Dimensional Structure of
626 Dendritic Spines and Synapses in Rat Hippocampus (CA1) at Postnatal Day 15 and Adult
627 Ages: Implications for the Maturation of Synaptic Physiology and Long-Term Potentiation.”
628 *The Journal of Neuroscience* 12(July): 2685–2705.

629 Hasegawa, Sho, Shigeo Sakuragi, Keiko Tominaga-yoshino, and Akihiko Ogura. 2015.
630 “Dendritic Spine Dynamics Leading to Spine Elimination after Repeated Inductions of LTD.”
631 *Scientific Reports*: 1–6.

632 Havrylenko, Svitlana et al. 2015. “WAVE Binds Ena / VASP for Enhanced Arp2 / 3 Complex –
633 Based Actin Assembly.” 26.

634 He, Siwei et al. 2015. “Transcriptional Control of Synaptic Remodeling through Regulated
635 Expression of an Immunoglobulin Superfamily Protein.” *Current Biology* 25(19): 2541–48.

636 He, Siwei, Andrea Cuentas-Condori, and David M Miller. 2019. “NATF (Native and Tissue-
637 Specific Fluorescence): A Strategy for Bright, Tissue-Specific GFP Labeling of Native
638 Proteins in *Caenorhabditis Elegans*.” *Genetics* (June).

639 Hering, Heike, Morgan Sheng, and Howard Hughes Medical. 2001. “Dendritic Spines :
640 Structure, Dynamics and Regulation.” 2(December): 880–88.

641 Ho, Hsin Yi Henry et al. 2004. “Toca-1 Mediates Cdc42-Dependent Actin Nucleation by
642 Activating the N-WASP-WIP Complex.” *Cell* 118(2): 203–16.

643 Honkura, Naoki et al. 2008. “The Subspine Organization of Actin Fibers Regulates the Structure
644 and Plasticity of Dendritic Spines.” *Neuron* 57(5): 719–29.

645 Hruska, Martin et al. 2018. “Synaptic Nanomodules Underlie the Organization and Plasticity of
646 Spine Synapses.” *Nature Neuroscience* 21(5): 671–82. [http://dx.doi.org/10.1038/s41593-](http://dx.doi.org/10.1038/s41593-018-0138-9)
647 [018-0138-9](http://dx.doi.org/10.1038/s41593-018-0138-9).

648 Kanjhan, Refik, Matthew J. Fogarty, Peter G. Noakes, and Mark C. Bellingham. 2016. 221 Brain
649 Structure and Function *Developmental Changes in the Morphology of Mouse Hypoglossal*
650 *Motor Neurons*. Springer Berlin Heidelberg.

651 Kanjhan, Refik, Peter G. Noakes, and Mark C. Bellingham. 2016. "Emerging Roles of Filopodia
652 and Dendritic Spines in Motoneuron Plasticity during Development and Disease." *Neural*
653 *Plasticity* 2016.
654 <http://www.embase.com/search/results?subaction=viewrecord&from=export&id=L6080430>
655 [14%0Ahttp://dx.doi.org/10.1155/2016/3423267%0Ahttp://resolver.ebscohost.com/openurl?](http://dx.doi.org/10.1155/2016/3423267)
656 [sid=EMBASE&issn=16875443&id=doi:10.1155%2F2016%2F3423267&atitle=Emerging+rol](http://resolver.ebscohost.com/openurl?sid=EMBASE&issn=16875443&id=doi:10.1155%2F2016%2F3423267&atitle=Emerging+rol)
657 [es+of+filopodi.](http://resolver.ebscohost.com/openurl?sid=EMBASE&issn=16875443&id=doi:10.1155%2F2016%2F3423267&atitle=Emerging+rol)

658 Kim, I H et al. 2013. "Disruption of Arp2/3 Results in Asymmetric Structural Plasticity of Dendritic
659 Spines and Progressive Synaptic and Behavioral Abnormalities." *J Neurosci* 33(14): 6081–
660 92. <http://www.ncbi.nlm.nih.gov/pubmed/23554489>.

661 Knott, Graham W., Charles Quairiaux, Christel Genoud, and Egbert Welker. 2002. "Formation of
662 Dendritic Spines with GABAergic Synapses Induced by Whisker Stimulation in Adult Mice."
663 *Neuron* 34(2): 265–73.

664 Korobchevskaya, Kseniya, B Christoffer Lagerholm, Huw Colin-york, and Marco Fritzsche.
665 2017. "Exploring the Potential of Airyscan Microscopy for Live Cell Imaging."

666 Kozorovitskiy, Yevgenia et al. 2005. "Experience Induces Structural and Biochemical Changes
667 in the Adult Primate Brain." *Proceedings of the National Academy of Sciences* 102(48):
668 17478–82.

669 Kubota, Y. et al. 2007. "Neocortical Inhibitory Terminals Innervate Dendritic Spines Targeted by
670 Thalamocortical Afferents." *Journal of Neuroscience* 27(5): 1139–50.

671 Kurup, Naina, and Yishi Jin. 2016. "Neural Circuit Rewiring: Insights from DD Synapse
672 Remodeling." *Worm* 5(1): e1129486. <http://www.ncbi.nlm.nih.gov/pubmed/27073734>.

673 Lee, Kevin F.H., Cary Soares, Jean Philippe Thivierge, and Jean Claude Béïque. 2016.

674 “Correlated Synaptic Inputs Drive Dendritic Calcium Amplification and Cooperative
675 Plasticity during Clustered Synapse Development.” *Neuron* 89(4): 784–99.

676 Leiss, Florian et al. 2008. “Characterization of Dendritic Spines in the Drosophila Central
677 Nervous System.” 1.

678 Lim, Maria A et al. 2016. “Neuroendocrine Modulation Sustains the C . Elegans Forward Motor
679 State.” : 1–33.

680 Lippi, Giordano et al. 2011. “Targeting of the Arpc3 Actin Nucleation Factor by MiR-29a/b
681 Regulates Dendritic Spine Morphology.” *Journal of Cell Biology* 194(6): 889–904.

682 Liu, Ping, Bojun Chen, and Zhao Wen Wang. 2013. “Postsynaptic Current Bursts Instruct Action
683 Potential Firing at a Graded Synapse.” *Nature Communications* 4(May): 1911.
684 <http://dx.doi.org/10.1038/ncomms2925>.

685 May-Britt, M., T. Mari, E. Thore, and A. Per. 1998. “Spatial Training in a Complex Environment
686 and Isolation Alter the Spine Distribution Differently in Rat CA1 Pyramidal Cells.” *Journal of*
687 *Comparative Neurology* 380(3): 373–81. [https://doi.org/10.1002/\(SICI\)1096-](https://doi.org/10.1002/(SICI)1096-9861(19970414)380:3%3C373::AID-CNE6%3E3.0.CO%0A2-#)
688 [9861\(19970414\)380:3%3C373::AID-CNE6%3E3.0.CO%0A2-#](https://doi.org/10.1002/(SICI)1096-9861(19970414)380:3%3C373::AID-CNE6%3E3.0.CO%0A2-#).

689 Mikhaylova, Marina et al. 2018. “Caldendrin Directly Couples Postsynaptic Calcium Signals to
690 Actin Remodeling in Dendritic Spines.” *Neuron* 97(5): 1110-1125.e14.

691 Mulcahy, Ben et al. 2018. “A Pipeline for Volume Electron Microscopy of the Caenorhabditis
692 Elegans Nervous System.” *Frontiers in Neural Circuits* 12(November).

693 Nance, Jeremy, and Christian Frøkjær-Jensen. 2019. 212 Genetics *The Caenorhabditis*
694 *Elegans Transgenic Toolbox*.
695 <http://www.genetics.org/lookup/doi/10.1534/genetics.119.301506>.

696 Nimchinsky, E, Bernardo L. Sabatini, and Karel Svoboda. 2002. “Structure and Function of
697 Dendritic Spines.” *Annu. Rev. Physiology*. 64: 313–53.

698 Noma, Kentaro, Alexandr Goncharov, Mark H Ellisman, and Yishi Jin. 2017. “Microtubule-
699 Dependent Ribosome Localization in C . Elegans Neurons.” (Dcc): 1–23.

700 Oliver, Devyn, Kellianne Alexander, and Michael M. Francis. 2018. "Molecular Mechanisms
701 Directing Spine Outgrowth and Synaptic Partner Selection in *Caenorhabditis Elegans*."
702 *Journal of Experimental Neuroscience* 12: 10–13.

703 Opperman, Karla J, and Brock Grill. 2014. "RPM-1 Is Localized to Distinct Subcellular
704 Compartments and Regulates Axon Length in GABAergic Motor Neurons." 9(1): 1–15.

705 Petersen, S. C. et al. 2011. "A Transcriptional Program Promotes Remodeling of GABAergic
706 Synapses in *Caenorhabditis Elegans*." *Journal of Neuroscience* 31(43): 15362–75.

707 Petralia, Ronald S., Nathalie Sans, Ya Xian Wang, and Robert J. Wenthold. 2005. "Ontogeny of
708 Postsynaptic Density Proteins at Glutamatergic Synapses." *Molecular and Cellular
709 Neuroscience* 29(3): 436–52.

710 Petralia, Ronald S, Ya-Xian Wang, Mark Mattson, and Pamela Yao. 2016. "The Diversity of
711 Spine Synapses in Animals." *NeuroMolecular Medicine* 18(4): 497–539.

712 Petrash, Hilary A et al. 2013. "ACR-12 Ionotropic Acetylcholine Receptor Complexes Regulate
713 Inhibitory Motor Neuron Activity in *Caenorhabditis Elegans*." 33(13): 5524–32.

714 Philbrook, Alison et al. 2018. "Neurexin Directs Partner-Specific Synaptic Connectivity in *C.
715 Elegans*." *eLife* 7: 1–30.

716 Pokala, N., Q. Liu, A. Gordus, and C. I. Bargmann. 2014. "Inducible and Titratable Silencing of
717 *Caenorhabditis Elegans* Neurons in Vivo with Histamine-Gated Chloride Channels."
718 *Proceedings of the National Academy of Sciences* 111(7): 2770–75.
719 <http://www.pnas.org/cgi/doi/10.1073/pnas.1400615111>.

720 Qi, Y. B. et al. 2012. "Photo-Inducible Cell Ablation in *Caenorhabditis Elegans* Using the
721 Genetically Encoded Singlet Oxygen Generating Protein MiniSOG." *Proceedings of the
722 National Academy of Sciences* 109(19): 7499–7504.
723 <http://www.pnas.org/cgi/doi/10.1073/pnas.1204096109>.

724 Riedl, Julia et al. 2008. "Lifeact: A Versatile Marker to Visualize F-Actin." *Nature methods* 5(7):
725 605–7.

726 Rochefort, Nathalie L., and Arthur Konnerth. 2012. "Dendritic Spines: From Structure to in Vivo
727 Function." *EMBO Reports* 13(8): 699–708. <http://dx.doi.org/10.1038/embor.2012.102>.

728 Rostaing, Philippe, Robby M Weimer, Erik M Jorgensen, and Antoine Triller. 2004.
729 "Preservation of Immunoreactivity and Fine Structure of Adult C . Elegans Tissues Using
730 High-Pressure Freezing The Journal of Histochemistry & Cytochemistry." *Histochemistry*
731 52(1): 1–12.

732 Sala, Carlo, and Menahem Segal. 2014. "Dendritic Spines: The Locus of Structural and
733 Functional Plasticity." : 141–88.

734 Schild, Lisa C., and Dominique A. Glauser. 2015. "Dual Color Neural Activation and Behavior
735 Control with Chrimson and CoChR in Caenorhabditis Elegans." *Genetics* 200(4): 1029–34.

736 Schindelin, Johannes et al. 2012. "Fiji: An Open-Source Platform for Biological-Image Analysis."
737 *Nature Methods* 9(7): 676–82.

738 Schindler, Adam J., and David R. Sherwood. 2013. "Morphogenesis of the Caenorhabditis
739 Elegans Vulva." *Wiley Interdisciplinary Reviews: Developmental Biology* 2(1): 75–95.

740 Scott, Ethan K, John E Reuter, and Liqun Luo. 2003. "Dendritic Development of Drosophila High
741 Order Visual System Neurons Is Independent of Sensory Experience." *BMC Neuroscience*
742 6: 1–6.

743 Soderling, Scott H et al. 2003. "Loss of WAVE-1 Causes Sensorimotor Retardation and
744 Reduced Learning and Memory in Mice." *Proceedings of the National Academy of*
745 *Sciences of the United States of America* 100(4): 1723–28.
746 <http://www.ncbi.nlm.nih.gov/pubmed/12578964>
747 <http://www.pubmedcentral.nih.gov/articlerender.fcgi?artid=PMC149900>.

748 Speese, Sean et al. 2007. "UNC-31 (CAPS) Is Required for Dense-Core Vesicle But Not
749 Synaptic Vesicle Exocytosis in Caenorhabditis Elegans." 27(23): 6150–62.

750 Spence, X Erin F, X Daniel J Kanak, Benjamin R Carlson, and Scott H Soderling. 2016. "The
751 Arp2 / 3 Complex Is Essential for Distinct Stages of Spine Synapse Maturation , Including

752 Synapse Unsilencing.” 36(37): 9696–9709.

753 Steward, O, T M Reeves, and M Reeves. 1988. “Protein-Synthetic Machinery beneath
754 Postsynaptic Sites on CNS Neurons: Association between Polyribosomes and Other
755 Organelles at the Synaptic Site.” *The Journal of neuroscience : the official journal of the
756 Society for Neuroscience* 8(1): 176–84. <http://www.ncbi.nlm.nih.gov/pubmed/3339407>.

757 Stretton, A O W et al. 1978. “Structure and Physiological Activity of the Motorneurons of the
758 Nematode *Ascaris*.” *Proceedings of the National Academy of Sciences, USA* 75(7): 3493–
759 97.

760 Takahashi, Naoya et al. 2012. “Locally Synchronized Synaptic Inputs.” *Science* 335(January):
761 353–57.

762 Taylor, Seth et al. 2019. “Expression Profiling of the Mature C. Elegans Nervous System by
763 Single-Cell RNA-Sequencing.” *BioRxiv*.

764 Trachtenberg, Joshua T et al. 2002. “Long-Term in Vivo Imaging of Experience-Dependent
765 Synaptic Plasticity in Adult Cortex.” *Nature* 420(19/26): 788–94.

766 ———. 2005. “Transient and Persistent Dendritic Spines in the Neocortex In Vivo.” *Neuron* 45:
767 279–91.

768 Umbriaco, Denis et al. 1994. “Ultrastructural and Morphometric Features of the Acetylcholine
769 Innervation in Adult Rat Parietal Cortex: An Electron Microscopic Study in Serial Sections.”
770 *Journal of Comparative Neurology* 348(3): 351–73.

771 Weimer, Robby M et al. 2006. “UNC-13 and UNC-10 Rim Localize Synaptic Vesicles to Specific
772 Membrane Domains.” *The Journal of neuroscience* 26(31): 8040–47.

773 Westphal, Ryan S et al. 2000. “Scar/WAVE-1 , a Wiskott-Aldrich Syndrome Protein , Assembles
774 an Actin-Associated Multi-Kinase Scaffold.” *The EMBO Journal* 19(17): 4589–4600.

775 White, John G., Albertson D. G., Anness M. A. R. “Connectivity Changes in a Class of
776 Motorneuron during Development of a Nematode.”

777 White, John G., D. G. Albertson, and M. Anness. 1978. “Connectivity Changes in a Class of

778 Motoneurone during the Development of a Nematode.” *Nature* 271: 764–66.

779 White, John G., E. Southgate, J. N. Thomson, and S. Brenner. 1976. “The Structure of the
780 Ventral Nerve Cord of *Caenorhabditis Elegans*.” *Philosophical Transactions of the Royal
781 Society B: Biological Sciences* 275.

782 ———. 1986. “The Structure of the Nervous System of the Nematode *Caenorhabditis Elegans*.”
783 *Philosophical Transactions of the Royal Society B: Biological Sciences* 314(1165): 1–340.
784 <http://rstb.royalsocietypublishing.org/cgi/doi/10.1098/rstb.1986.0056>.

785 Yuste, Rafael. 2015. “The Discovery of Dendritic Spines by Cajal.” 9(April): 1–6.

786 Zhen, Mei, Xun Huang, Bruce Bamber, and Yishi Jin. 2000. “Regulation of Presynaptic Terminal
787 Organization by *C. Elegans* RMP-1, a Putative Guanine Nucleotide Exchanger with a
788 RING-H2 Finger Domain.” *Neuron* 26: 331–43.

789 Zhou, Qiang, Koichi J. Homma, and Mu Ming Poo. 2004. “Shrinkage of Dendritic Spines
790 Associated with Long-Term Depression of Hippocampal Synapses.” *Neuron* 44(5): 749–57.

791 Zuo, Yi, Aerie Lin, Paul Chang, and Wen Biao Gan. 2005. “Development of Long-Term Dendritic
792 Spine Stability in Diverse Regions of Cerebral Cortex.” *Neuron* 46(2): 181–89.

793

794

795 **FIGURE LEGENDS**

796

797 **Figure 1. DD GABAergic neurons display dendritic spines.**

798 **A.** Six DD motor neurons are located in the *C. elegans* ventral nerve cord. In the adult, DD
799 presynaptic boutons (oblong ovals) innervate dorsal muscles (grey cells) and DD postsynaptic
800 termini (spines) receive cholinergic input from VA and VB motor neurons on the ventral side
801 (magenta).

802 **B-F.** Airyscan imaging resolves ventrally projecting spines from DD neurons labeled with **(B)**
803 cytosolic mCherry or **(C)** LifeAct::GFP. **D.** Intensity of spine over shaft ratio reveals that **(E)**
804 LifeAct::GFP preferentially accumulates at the spine whereas cytosolic mCherry is evenly
805 distributed between the spine and shaft (KS test, $p < 0.0001$, $n > 286$ spines). **F.** Spine density of
806 young adults revealed by mCherry (3.68 ± 0.8 spines/ $10\mu\text{m}$) or LifeAct::GFP (3.43 ± 1.2
807 spines/ $10\mu\text{m}$) is not significantly different (t test, $p = 0.0855$, $n > 16$ worms). Measurements are
808 mean \pm SD. Scale bars = $2\ \mu\text{m}$.

809 **G-I.** LifeAct::GFP reveals 1. Thin/Mushroom ($55.5 \pm 14.5\%$), 2. Filopodial ($10.3 \pm 8.70\%$), 3.
810 Stubby ($18.8 \pm 10.4\%$), 4. Branched spines ($15.4 \pm 6.0\%$) in adult DD motor neurons.
811 Measurements are mean \pm SD, $n = 16$ worms, 357 spines. For scatterplot, see Figure S1.
812 (Scale bar = $1\ \mu\text{m}$).

813 **H.** Schematic of spine shapes.

814 **I.** Images of each type of spine identified by (top) Airyscan imaging (Scale bar = 500nm) of
815 LifeAct::GFP or (bottom) 3D-reconstruction of DD1 from serial electron micrographs of a high-
816 pressure frozen young adult. See also Figure S1B.

817 **J.** Dendritic spines are dynamic. Snapshots of *in vivo* spine remodeling from a thin/mushroom
818 (arrowhead) to branched morphology (arrow). Images (LifeAct::GFP) are shown with a rainbow
819 LUT. Higher intensity is represented by warm colors and dimmer intensity by cold colors. L4
820 stage larva. See also Figure S1C-H. Scale bar = $500\ \text{nm}$

821

822 **Figure 2. DD spines appose presynaptic cholinergic vesicles**

823 **A.** Postsynaptic ionotropic acetylcholine receptors (iAChRs) are localized in GABAergic motor
824 neurons in apposition to input from cholinergic motor neurons.

825 **B.** Cholinergic RAB-3 presynaptic vesicles labeled with mCherry localize in close proximity to
826 DD postsynaptic spines labeled with *flp-13::LifeAct::GFP*. Young adult stage worms. Scale bar =
827 1µm. Asterisk denotes the DD cell body. Arrowheads mark multiple RAB-3::mCherry clusters
828 apposing dendritic spines.

829 **C.** Volumetric EM reconstruction of a portion of the DD1 dendrite (25 µm) in the ventral nerve
830 cord (gray) detects contacts with 43 presynaptic termini from axons of the cholinergic (VA1,
831 VA2, VB2) and GABAergic (VD) motor neurons, and other neurons (other). 84.8% (n=28/33) of
832 VA and VB inputs are adjacent to DD spines. 33.3% (4/12) of spines directly oppose a single
833 presynaptic partner (black arrowhead); the majority of spines (66.7%) appose more than one
834 terminal (clear arrowhead). Scale bar = 2 µm.

835 **D.** Frequency of spines contacted by cholinergic presynaptic sites detected by Airyscan imaging
836 (contacted, 84.1 ± 6.4% vs not contacted, 15.8 ± 6.4%, n = 128 spines from 7 worms) or by EM
837 (contacted, 100% vs not contacted, 0%, n = 12 spines from 1 worm).

838 **E.** Schematic of DD presynaptic boutons (top) and postsynaptic spines (dashed box) with distal
839 iAChR puncta (green dots) on the ventral side.

840 **F1-3.** iACh receptor subunit ACR-12::GFP (green) localizes to LifeAct::mCherry-labeled DD
841 spines (magenta). Asterisk marks DD cell body. Arrows in F1 denote spines without visible ACR-
842 12::GFP clusters. Scale bars = 1 µm.

843 **G-H.** Locations of ACR-12::GFP puncta on DD spines. > 95% of spines have at least one ACR-
844 12::GFP cluster (n = 127 spines from 8 young adult worms). Examples of spines from each
845 category. Scale bars = 1 µm. **(H)** Examples of spines with more than one ACR-12::GFP cluster.
846 White arrowheads point to ACR-12::GFP clusters at DD spines. Scale bar = 200 nm.

847 **I-K.** NATF labeling of endogenous iAChR auxiliary protein LEV-10 in DD neurons (**I**) detects
848 LEV-10 localization to spines with (**J**) all spines showing NATF LEV-10::GFP puncta (n = 159
849 spines from 7 worms). Scale bars = 500 nm. (**K**) Example of spines with endogenous LEV-10
850 clusters. Scale bar = 200 nm.

851

852 **Figure 3. SER-like structures and ribosomes in spines and dendritic shaft.**

853 **A.** 3D EM reconstruction of DD1 dendrite reveals Smooth Endoplasmic Reticulum (SER)-like
854 cisternae (yellow) in the dendritic shaft and some spines (black arrowheads). Most spines lack
855 SER-like structures (clear arrowheads). Scale bar = 2 μ m.

856 **B.** Serial cross-sections (328-355) of the ventral nerve cord show spines (Sp) budding from DD1
857 (blue) dendritic shaft (Sf). 'Pre' labels presynaptic terminals from a cholinergic VA neuron (pink);
858 m, muscle arm (purple). (Scale bar = 200 nm) **B'**. Magnified region of section 332. Arrow points
859 to SER-like structure in DD dendritic spine (Scale bar = 100 nm). **B''**. Section 333. Arrow points
860 to polysome-like structure in DD dendritic spine (Scale bar = 100 nm). **B'''**. Volumetric
861 reconstruction of DD1 dendrite (gray) and SER-like structures (yellow). Dashed lines denote
862 location of each section shown in B. Scale bar = 500 nm.

863 **C.** Airyscan imaging shows GFP-labeled ribosomal protein, RPS-18 (Noma et al. 2017),
864 localized to DD spines (arrowheads) labeled with LifeAct::mCherry. Scale bar = 2 μ m.

865 **D.** Volumetric EM reconstruction of a portion of the DD1 (25 μ m) dendrite shows mitochondria
866 (purple) in the shaft (arrowheads) but not in spines (clear arrowheads).

867

868 **Figure 4. Coordinated Ca⁺⁺ transients in dendritic spines.**

869 Series (time in seconds) of live-cell images of cytosolic (**A**) mCherry and (**B**) GCaMP6s in DD
870 postsynaptic spines reveals (**C**) dynamic GCaMP6s vs stable mCherry signals, n = 11 movies,
871 31 spines. **D.** GCaMP6s transients occur in neighboring spines more frequently (> 50%) than
872 predicted by a random distribution (KS test, p<0.0001). Scale bars = 500 nm.

873 **E-H.** VA motor neuron activation is correlated with Ca^{++} transients in DD1 spines. GCaMP6s
874 fluorescence imaged (at 0.5 sec intervals) with periodic optogenetic activation (at 2.5 sec
875 intervals) of ceChrimson, detects Ca^{++} transients with **(E)** ATR (n = 14) but not with carrier **(F)**
876 (EtOH) (n = 12). Circles at the top right corner of each panel correspond to red light on (red) for
877 ceChrimson activation vs off (black). Scale bars = 500 nm. **(G)** GCaMP6s fluorescence
878 throughout the 15 sec recording period plotted for ATR (green) (n = 14) vs carrier (EtOH) (black)
879 (n = 12). **(H)** Plot of the standard deviation (SD) of GCaMP6s signal at each time-point shows
880 that fluctuations in the ATR-treated samples (green boxes) are significantly greater than in EtOH
881 controls (black circles), F-test, $\ast = p < 0.0001$. Additionally, SDs are significantly different
882 between timepoints before and after light activation (T_6 vs T_7 and T_{11} vs. T_{12}). F-test, $\wedge = p <$
883 0.05 . ND = not determined. Purple bars denote interval with red-light illumination (e.g.,
884 ceChrimson activation).

885 **I-K.** Ca^{++} propagation to neighboring spines depends on intracellular Ca^{++} stores. **(I)** Graphical
886 representation of the experimental paradigm: 561nm laser excitation at a single spine (excitation
887 area, pink) with subsequent GCaMP6s changes recorded from three different regions of interest
888 at: (1) the excited spine, (2) an adjacent spine and (3) a distant spine. **(J)** In the wild type,
889 significant Ca^{++} changes are detected at the excited spine ($p = 0.0182$), adjacent spine ($p =$
890 0.0319) and distant spine ($p = 0.0402$), n = 15 videos. **(K)** In ryanodine-treated worms,
891 significant Ca^{++} changes are not detected at the excited spine ($p > 0.999$), at an adjacent spine
892 ($p = 0.924$) or at a distant spine ($p = 0.552$), n = 16 videos.

893

894 **Figure 5. Cholinergic activity regulates spine density during development.**

895 **A.** Synaptic vesicles are loaded with acetylcholine (ACh) by the vesicular acetylcholine
896 transporter (vAChT/UNC-17). Acetylcholinesterase enzymes (ACE) degrade synaptic ACh.

897 **B-E.** Spine density increases throughout development in the wild type (WT) but not in *unc-*
898 *17(e113)* mutants whereas spine density is precociously elevated in *ace-1(p1000);ace-2(g72)*

899 mutants. Representative images of **(B)** WT, **(C)** *unc-17 (e113)* and **(D)** *ace-1(p100); ace-2(g72)*.

900 Scale bars = 2 μ m. See Figure S4 for scatter plots for **E**.

901 **F-I**. Reduced ACh signaling in cholinergic motor neurons decreases postsynaptic spine density.

902 **F**. Expression of Histamine-gated Chloride channels and mCherry in cholinergic (VA and DA)

903 motor neurons (*punc4::HisCl::SL2::mCherry*) (Pokala et al. 2014) vs DD motor neurons labeled

904 with LifeAct::GFP shows **(G)** DD spines (green) extending to the ventral process of the VA5

905 motor neuron (magenta). Note dorsal placement of DA4 axon.

906 **H**. Synchronized L2 larvae were transferred to either histamine or control plates at T_{29} (hours

907 post-laying) for growth up to the L4 stage ($\sim T_{50}$), See Methods.

908 **I**. DD spine density at the L4 stage is reduced by growth on histamine (2.58 ± 0.6) vs control

909 (3.49 ± 0.9). T-test, ** = $p < 0.01$, $n > 17$. Scale bars = 1 μ m.

910 **J-M**. Temporal activation of A-class cholinergic motor neurons increases spine density.

911 **J**. Cholinergic motor neurons (e.g., VA4) express ceChrimson (Schild and Glauser 2015) and

912 mCherry (*punc4::ceChrimson::SL2::mCherry*). LifeAct::GFP marks DD2.

913 **K**. DD spines (green) extend ventrally toward VA process (magenta).

914 **L**. Synchronized L2 stage larvae (T_{27} , hours post-laying) were transferred to ATR or control

915 plates (see Methods) for 6 hours (until T_{33} , \sim L3 stage) and exposed to red-light pulses vs control

916 group grown in the dark.

917 **M**. Exposure to red-light for 6 hours elevates spine density at the L3 stage (3.9 ± 0.8) vs control

918 (2.59 ± 0.8). T-test, *** is $p < 0.001$, $n > 10$. Scale bars = 1 μ m.

919

920 SUPPLEMENTARY INFORMATION

921

922 **Figure 1 – Figure Supplement 1. Dendritic spines adopt distinct morphologies.**

923 **A**. Spine densities determined from young adult DD neurons labeled with mCherry (3.68 ± 0.8

924 spines/10 μ m), LifeAct::GFP (3.43 ± 1.2 spines/10 μ m) and MYR::mRuby (3.09 ± 0.8

925 spines/10 μ m) are not significantly different and are comparable to spine density determined by
926 3D EM reconstruction of DD1 (4.2 spines/10 μ m) (dashed blue line). One-way ANOVA between
927 mCherry, LifeAct::GFP and MYR::mRuby ($p > 0.05$), $n > 16$. Data for mCherry and LifeAct::GFP
928 also appears in Figure 1F.

929 **B.** Example of DD spines labeled with membrane bound marker, myristolated mRuby
930 (MYR::mRuby).

931 **C.** Frequency of spines by type labeled with LifeAct::GFP: Thin/Mushroom ($55.5 \pm 14.5\%$),
932 Filopodial ($10.3 \pm 8.70\%$), Stubby ($18.8 \pm 10.7\%$), Branched ($15.4 \pm 6.01\%$). Dashed blue lines
933 denote frequency for each spine type from EM reconstruction of DD1: Thin/Mushroom (58.3%),
934 Filopodial (25%), Branched (8.3%) and Stubby (8.3%).

935 **D.** Frequency of spines by type, labeled with MYR::mRuby: Thin/Mushroom ($52.2 \pm 16.5\%$),
936 Filopodial ($5.68 \pm 7.0\%$), Stubby ($33.1 \pm 14.8\%$), Branched ($9.02 \pm 9.6\%$). Unpaired T-test
937 shows that frequency of Filopodial ($p = 0.0339$); Stubby ($p = 0.0009$) and Branched ($p = 0.011$)
938 classes labeled with MYR::mRuby is differs from frequency of spine types detected with with
939 LifeAct::GFP labeling. Data for LifeAct::GFP labeled spines also shown in Figure S1C.

940

941 **Figure 1 – Figure Supplement 2. Dendritic spines display a dynamic actin cytoskeleton.**

942 **A-E.** Live-imaging of **(A,B)** LifeAct::GFP and **(C,D)** mCherry-labeled DD spines of L4 stage
943 larvae reveals dynamic LifeAct::GFP vs stable cytosolic mCherry signals.

944 **B,D.** Normalized traces of LifeAct::GFP and mCherry fluorescence from live imaging. Different
945 shades of green and red lines are used to allow visualization of individual traces. **E.** Comparison
946 of standard deviations of all traces for each timepoint reveals significantly different variance
947 between LifeAct::GFP vs cytosolic mCherry markers (F-test, * is $p < 0.0001$ from T_3 to T_{30} and \$
948 is $p < 0.05$ at T_{39} , $n > 51$ traces). Scale bar = 500 nm.

949 **F.** Regulators of actin polymerization define spine density. (Left) Representative images (young
950 adults) of DD spines for WT (wild type), *toca-1* (*tm2056*), empty vector (RNAi control),

951 *wave/wve-1*(component of WRC) RNAi and *p21/ax-5* (component of Arp2/3 complex) RNAi.
952 (Right) WT young adults show 3.53 ± 1.0 spines/10 μ m vs *toca-1 (tm2056)* with 2.77 ± 1.1
953 spines/10 μ m (t test, *** is $p < 0.001$). Spine density is reduced with RNAi of *wave/wve-1* ($2.24 \pm$
954 0.7 spines/10 μ m) or *p21/ax-5* RNAi (2.20 ± 0.7 spines/10 μ m) versus Empty Vector (E.V.)
955 control (2.9 ± 0.4 spines/10 μ m). One-way ANOVA with Dunnett's multiple comparison test, ** is
956 $p < 0.01$, $n > 9$ worms. Measurements are Mean \pm SD. Scale bar is 1 μ m.

957 **G.** TOCA-1 functions cell-autonomously in DD neurons. wild-type young adults show 3.53 ± 1.0
958 spines/10 μ m vs 2.35 ± 0.9 spines/10 μ m in *toca-1(tm2056)*, which is rescued with TOCA-1a
959 expression in DD neurons (*Pflp-13::TOCA-1a::mCherry*) = 3.05 ± 0.8 spines/10 μ m. One-way
960 ANOVA with Dunnett's multiple comparison test. n.s.= not significant. ** is $p < 0.01$. wild type
961 and *toca-1(tm2056)* data also appears in Figure S2F.

962

963 **Figure 4 – Figure Supplement 1. Dendritic Ca⁺⁺ transients depend on intracellular Ca⁺⁺**
964 **stores.**

965 **A.** Intrinsic GCaMP6s transients are dramatically reduced in *unc-68(r1142)* mutants.

966 Neither **(B)** Control (EtOH only) or **(C)** ryanodine-treated (ryanodine + EtOH) worms show
967 significant Ca⁺⁺ changes after 561nm local excitation ($n > 6$ videos).

968

969 **Figure 5 – Figure Supplement 1. Synaptic activity regulates postsynaptic DD spine**
970 **density.**

971 **A.** Spine density (spines/10 μ m) increases throughout development in the wild type (WT). L3
972 (2.5 ± 0.9), (early L4) eL4 (3.1 ± 0.9), L4 (3.4 ± 0.9) and (Young Adult) YA (3.4 ± 1.1). One-way
973 ANOVA of all groups vs L3 shows that spine densities at L4 and YA stages are different from
974 L3. *** is $p < 0.001$. Data for YA are the same as in Figure 1F and S1A for wild-type
975 LifeAct::GFP.

976 **B.** Spine density (spines/10 μm) does not increase during development with reduced cholinergic
977 signaling in *unc-17(e113)*. L3 (2.91 ± 1.0), eL4 (2.76 ± 0.9), L4 (2.32 ± 0.87) and YA ($2.84 \pm$
978 0.9). One-way ANOVA of all groups against L3 stage shows no statistically significant difference
979 during development.

980 **C.** Spine density (spines/10 μm) is elevated throughout development in acetylcholinesterase
981 deficient *ace-1(p100);ace-2(g72)* mutant animals. L3 (3.83 ± 1.2), eL4 (4.17 ± 0.8), L4 ($3.16 \pm$
982 1.2) and YA (3.49 ± 1.1). One-way ANOVA of all groups against L3 stage shows no statistically
983 significant difference during development.

984 **D.** Spine density (spines/10 μm) does not increase during development in *unc-31(e169)* mutants
985 with impaired dense core vesicle release L3 (2.18 ± 1.0), eL4 (2.45 ± 1.1), L4 (2.65 ± 0.9) and
986 YA (1.89 ± 0.8). One-way ANOVA of all groups against L3 stage shows no statistically
987 significant difference during development.

988 **E.** Spine density (spines/10 μm) does not increase during development in *unc-31(e169)* and
989 shows lower spine density than wild type (WT) at the Young Adult (YA) stage. T-test at each
990 timepoint between genotypes, **** is $p < 0.0001$. Measurements are mean \pm SD.

991

992 **Figure 5 – Figure Supplement 2. Ventral D-GABAergic motor neurons have dendritic**
993 **spines**

994 **A.** VD motor neurons (green) are located in the ventral nerve cord. In the adult, VD presynaptic
995 boutons (oblong ovals) innervate ventral muscles (gray cells) and VD postsynaptic termini
996 (spines) receive cholinergic input from DA and DB motor neurons (magenta) on the dorsal side.

997 **B-D.** GABAergic VD neurons show dendritic spines. GABA neurons were labeled with
998 LifeAct::GFP (*Punc-25::LifeAct::GFP*) and DD neurons expressed miniSOG (*Pflp-*
999 *13::miniSOG::SL2::BFP*).

1000 **B.** Synchronized L1 larvae were exposed to blue light for 45 minutes during T₁₆-T₁₇ (hours after
1001 egg laying) to ablate DD neurons and maintained at 20°C until the adult stage.

1002 **C.** Airyscan imaging of the dorsal cord in young adults (T_{60}) (hours after egg laying) shows
1003 spine-like protrusions on VD neurons.

1004 **C'.** Inset from **C**. Scale bars = 1 μm .

1005 **D.** VD spine density (3.01 ± 1.43 spines/ $10\mu\text{m}$), $n = 17$. Dashed blue line represents spine
1006 density detected in VD2 with 3D EM (3.33 spines/ $10\mu\text{m}$).

1007 **E.** 3D EM reconstruction shows mitochondria in the shaft of VD dendrites (arrows) but not in VD
1008 spines (clear arrowheads).

1009 **F.** Volumetric EM reconstruction of a portion of the VD2 dendrite ($27 \mu\text{m}$) in the dorsal nerve
1010 cord (gray) detects contacts with 36 presynaptic termini from axons of the cholinergic (DA, DB
1011 or AS) and GABAergic (DD) motor neurons. 50.0% ($n=11/22$) of DA and DB inputs are adjacent
1012 to VD spines. 44.4% ($4/9$) of spines directly oppose a single presynaptic partner (black
1013 arrowhead) or more than one terminal (clear arrowhead). One VD spines does not appose any
1014 presynaptic density (gray arrowhead). Scale bar = 2 μm .

1015

1016 **VIDEO DESCRIPTIONS**

1017

1018 **Video 1. *In vivo* spine dynamics**

1019 A thin spine extends a lateral projection to form a branched spine. Snapshots are displayed in
1020 Figure 1J. Pseudo-colored with Rainbow Dark LUT.

1021

1022 **Video 2. LifeAct::GFP dynamics**

1023 LifeAct::GFP fluorescence at DD spines (white arrows) fluctuates between bright and dark
1024 signals. Asterisk labels DD cell body and yellow arrow labels transient protrusion and
1025 commissures. Scale bar = 5 μm . Pseudo-colored with Rainbow Dark LUT.

1026

1027 **Video 3. Cytosolic mCherry dynamics**

1028 Cytosolic mCherry at DD spines (white arrows) shows modest changes in fluorescence over
1029 time. Yellow arrows label transient protrusions and commissures. Scale bar = 5 μm . Pseudo-
1030 colored with Rainbow Dark LUT.

1031

1032 **Video 4. DD1 dendritic spine receives input from cholinergic neurons**

1033 3D EM reconstruction shows that a single DD spine (gray) contacts presynaptic terminals of VA
1034 (blue) and VB (pink) neuron. Muscle arms labeled in green.

1035

1036 **Video 5. 3D EM reconstruction of DD1 dendrite**

1037 DD1 dendrite (gray) has dendritic spines that contain ER (yellow) but no mitochondria (pink).

1038

1039 **Video 6. Intrinsic Ca^{++} waves in DD spines.**

1040 GCaMP6s (green, center panel) detects spontaneous Ca^{++} transients in the DD1 dendritic shaft
1041 and spines (arrows). Note the relatively constant cytosolic mCherry signal (magenta, left panel)
1042 GCaMP6s and mCherry signals are merged in the right panel. Scale bar = 2 μm . Pseudo-
1043 colored with Rainbow Dark LUT.

1044

1045 **Video 7. Cholinergic activation triggers Ca^{++} transients in DD spines**

1046 Three examples of GCaMP6s changes recorded with activation of cholinergic neurons every 2.5
1047 seconds (pink circle) on ATR-grown worms. Scale bar = 2 μm . Pseudo-colored with Rainbow
1048 Dark LUT. Arrows denote spines.

1049

1050 **Video 8. Cholinergic activation does not trigger large changes in cytosolic Ca^{++} in DD
1051 spines in the absence of ATR.**

1052 Three examples of GCaMP6s changes recorded after activation of cholinergic neurons every
1053 2.5 seconds (pink circle) in control worms grown in the absence of ATR. Scale bar = 2 μm .

1054 Pseudo-colored with Rainbow Dark LUT. Arrows denote spines. Asterisk (left panel) marks DD
1055 neuron soma.

1056

1057 **Video 9. Local cholinergic activation triggers Ca⁺⁺ transients in neighboring spines**

1058 Top: Activation of cholinergic neurons at a single spine (white arrow) triggers Ca⁺⁺ changes at
1059 adjacent (red arrow) and distant spines (yellow). ceChrimson::SL2::3xNLS::GFP labels DA and
1060 VA nuclei in green (black asterisks). The DD1 cell soma is labeled. Scale bar = 5 μm.

1061 Bottom: Traces of local Ca⁺⁺ changes at excited (red), adjacent (white) and distant (yellow)
1062 spines over time. Vertical yellow bar denotes the 561nm excitation window. Note that GCaMP6s
1063 signals during the period of 561 nm excitation are interpolated from signals measured
1064 immediately before and after excitation.

1065

1066 **SOURCE DATA FILES**

1067

1068 **Data for Figure 1E**

1069 Individual measurements of spines/shaft intensity ratios labeled with cytosolic mCherry or
1070 LifeAct::GFP.

1071

1072 **Data for Figure 1F and Figure Supplement 1A**

1073 Density (in 10 μm) of spines labeled with Cytosolic mCherry, LifeAct::GFP or MYR::mRuby.

1074

1075 **Data for Figure 1 – Figure Supplement 1C-1D.**

1076 Frequency of spines by type (i.e. Thin/Mushroom, Stubby, Filopodial and Stubby) labeled with
1077 LifeAct::GFP or MYR::mRuby.

1078

1079 **Data for Figure 3C**

1080 Number of spines labeled with LifeAct::mCherry and proportion that are also marked with
1081 DD::RIBOS (*Pflp-13::GFP::RPS-18*) (Noma et al. 2017) to visualize ribosomes.

1082

1083 **Data for Figure 4A-C**

1084 Cytosolic mCherry and GCaMP6s normalized fluorescence sampled every 2 seconds to detect
1085 intrinsic Ca⁺⁺ changes in DD dendrites.

1086

1087 **Data for Figure 4E-H**

1088 Cytosolic mCherry and GCaMP6s normalized fluorescence sampled every 200 ms to detect
1089 Ca⁺⁺ changes in response to 561 nm activation on the field of view.

1090

1091 **Data for Figure 4I-K and Figure Supplement 1B-C**

1092 Normalized GCaMP6s fluorescence sampled every 2 s to detect Ca⁺⁺ changes in response to
1093 561 nm activation at a single spine. GCaMP6s changes were recorded at the excited spine,
1094 neighboring spine and distant spine in the presence or absence of ATR (i.e. ATR or EtOH) with
1095 or without 1mM Ryanodine.

1096

1097 **Data for Figure 5B-E and Figure Supplement 1**

1098 Spine density for wild type and synaptic mutants (i.e. *unc-17*, *ace-1;ace-2* and *unc-31*) across
1099 four different developmental stages (L3, early L4, L4 and Young Adult).

1100

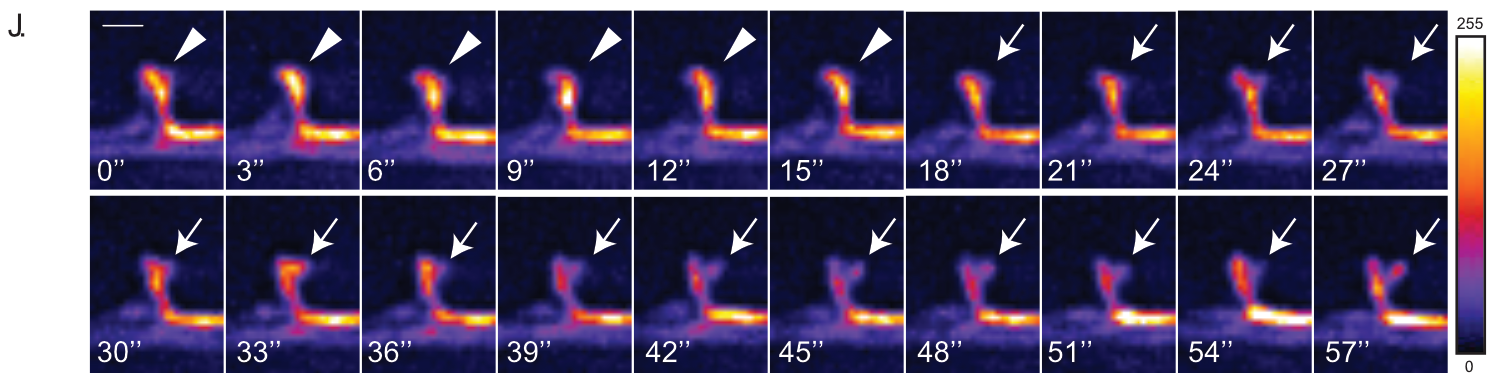
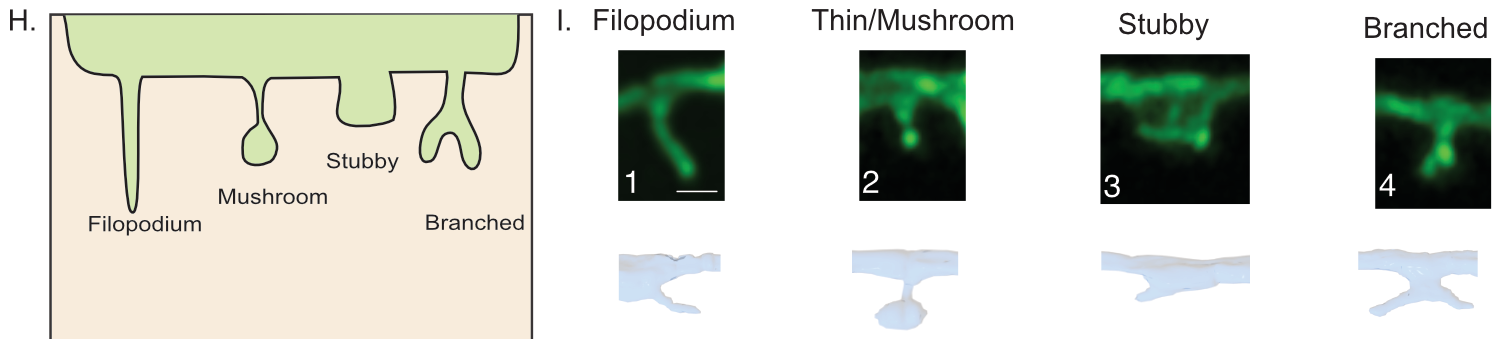
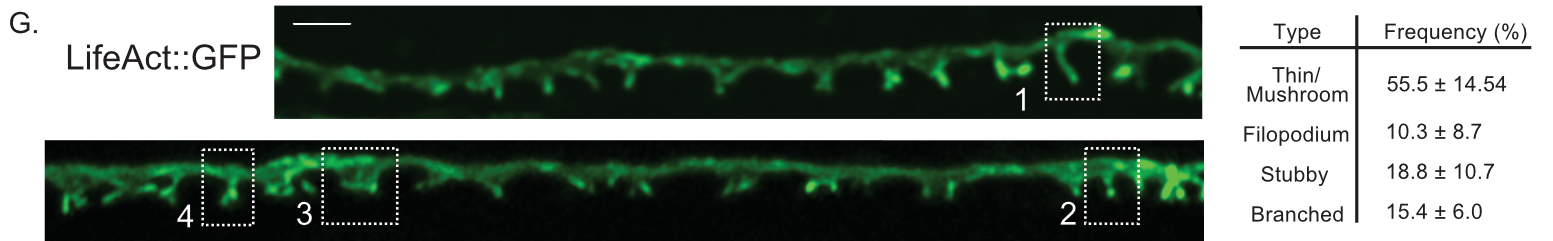
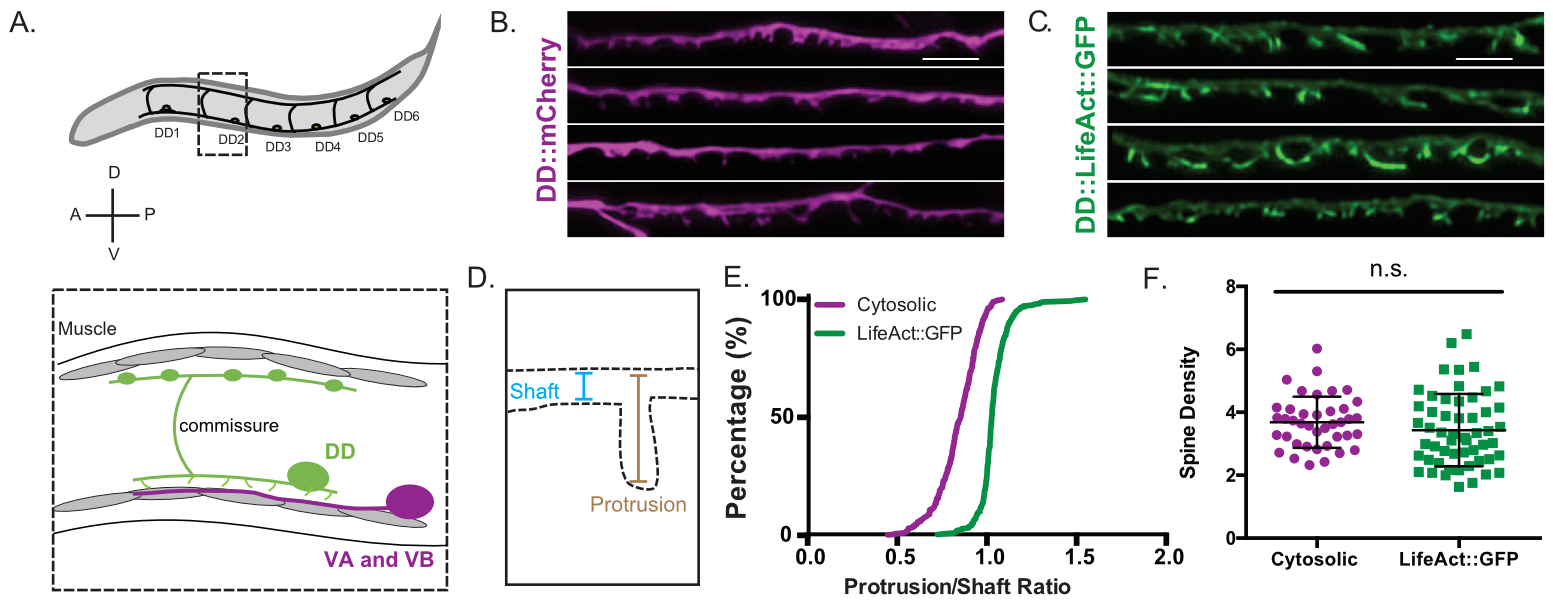
1101 **Data for Figure 5F-K**

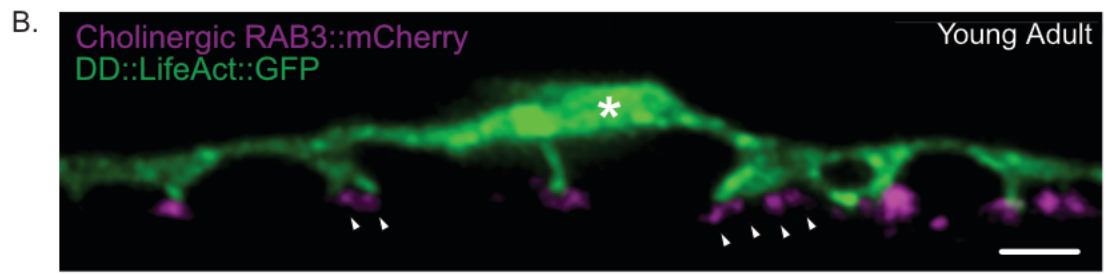
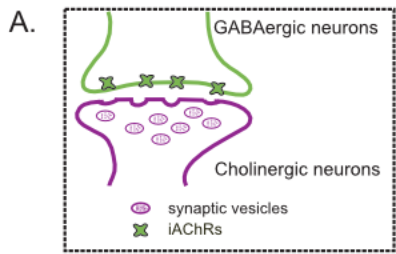
1102 Spine density recorded after temporal elevation of cholinergic activity (*Punc-*
1103 *4::ceChrimson::SL2::mCherry*) or decrease (*Punc-4::HisCL::SL2::mCherry*).

1104

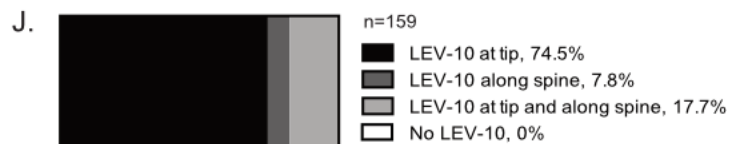
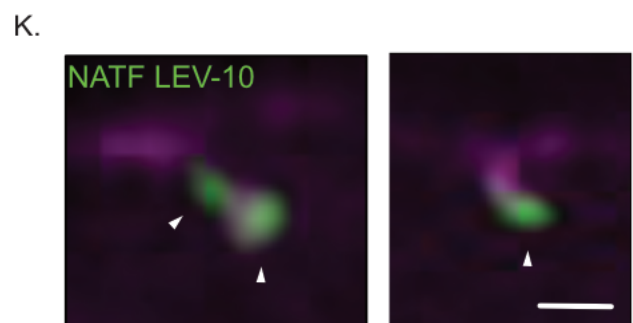
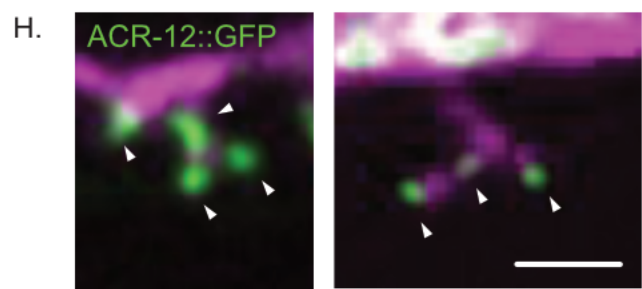
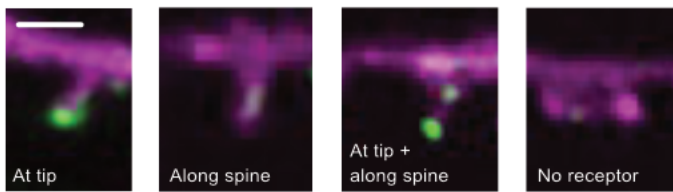
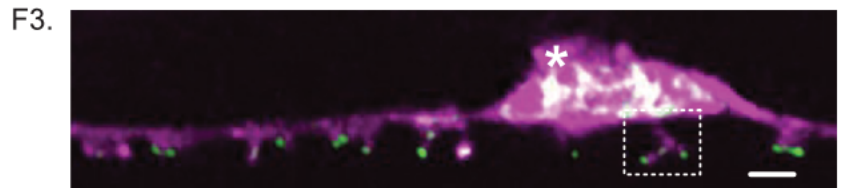
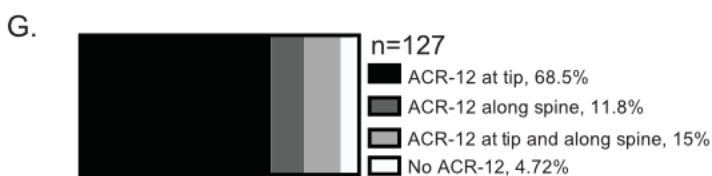
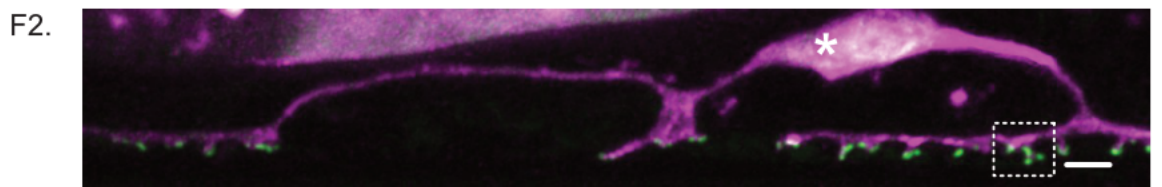
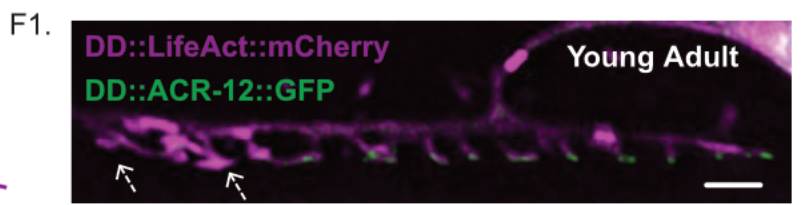
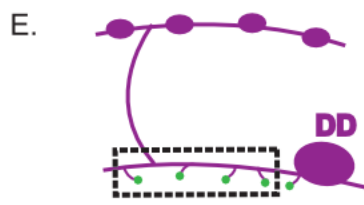
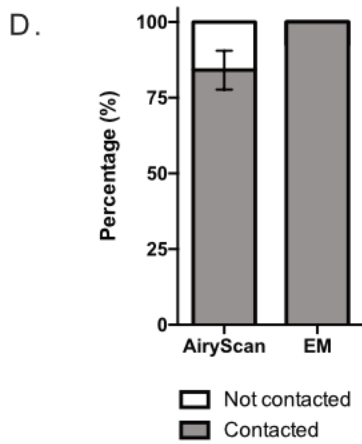
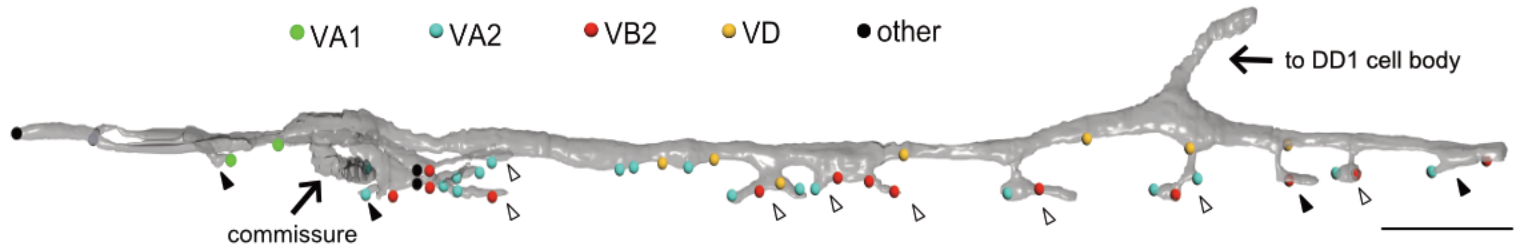
1105 **Data for Figure 5 - Figure Supplement 2**

1106 Spine density of VD neurons labeled with *Punc-25::LifeAct::GFP* (See Methods).

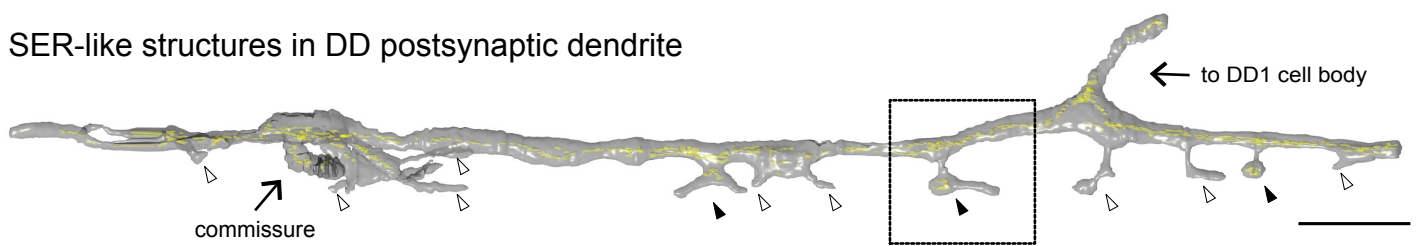




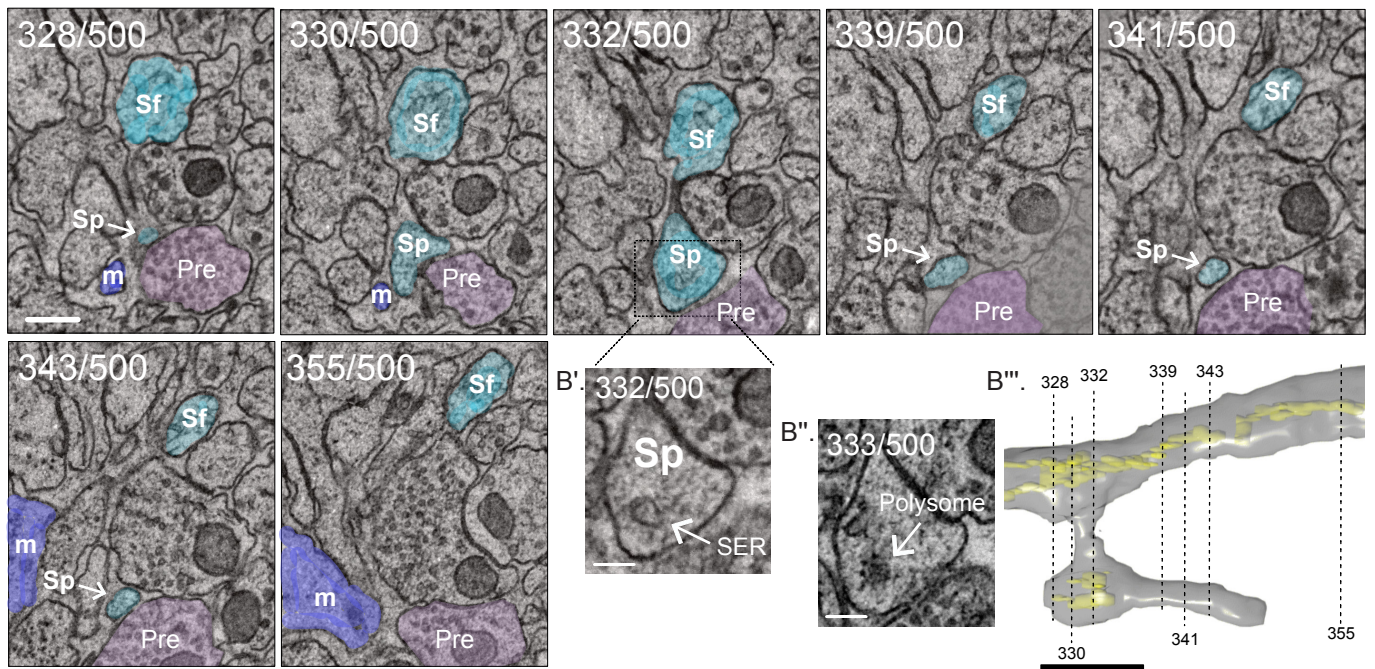
C. Synaptic input onto DD postsynaptic dendrite



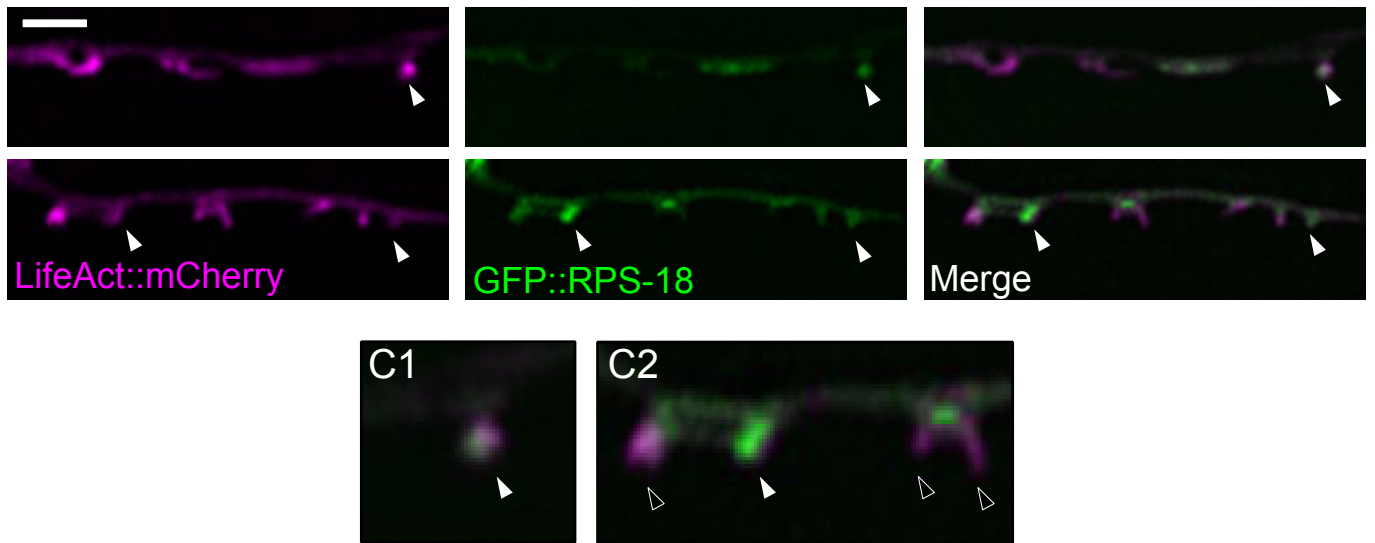
A. SER-like structures in DD postsynaptic dendrite



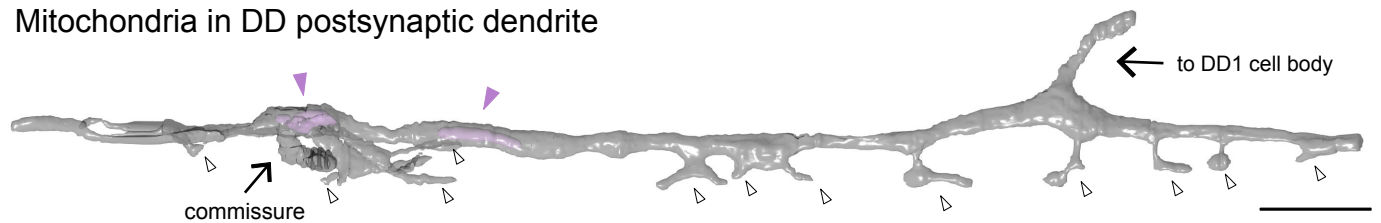
B.

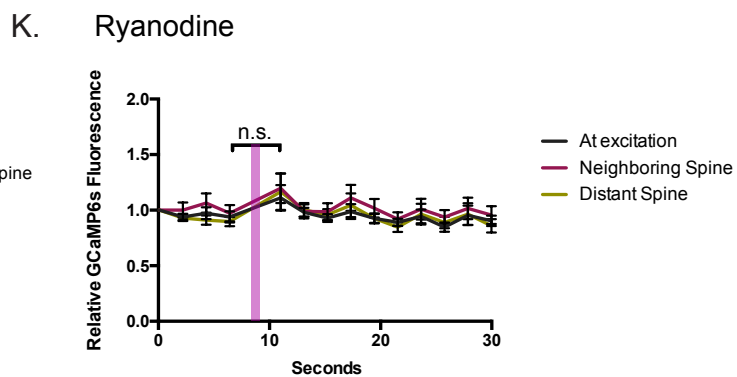
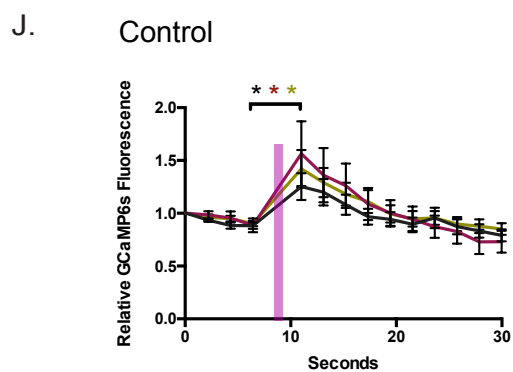
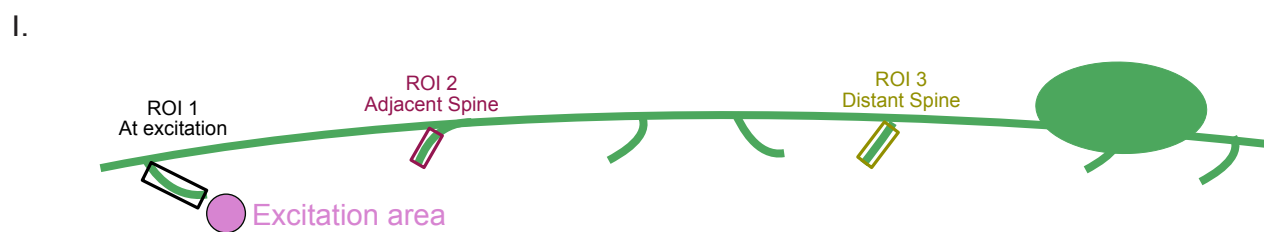
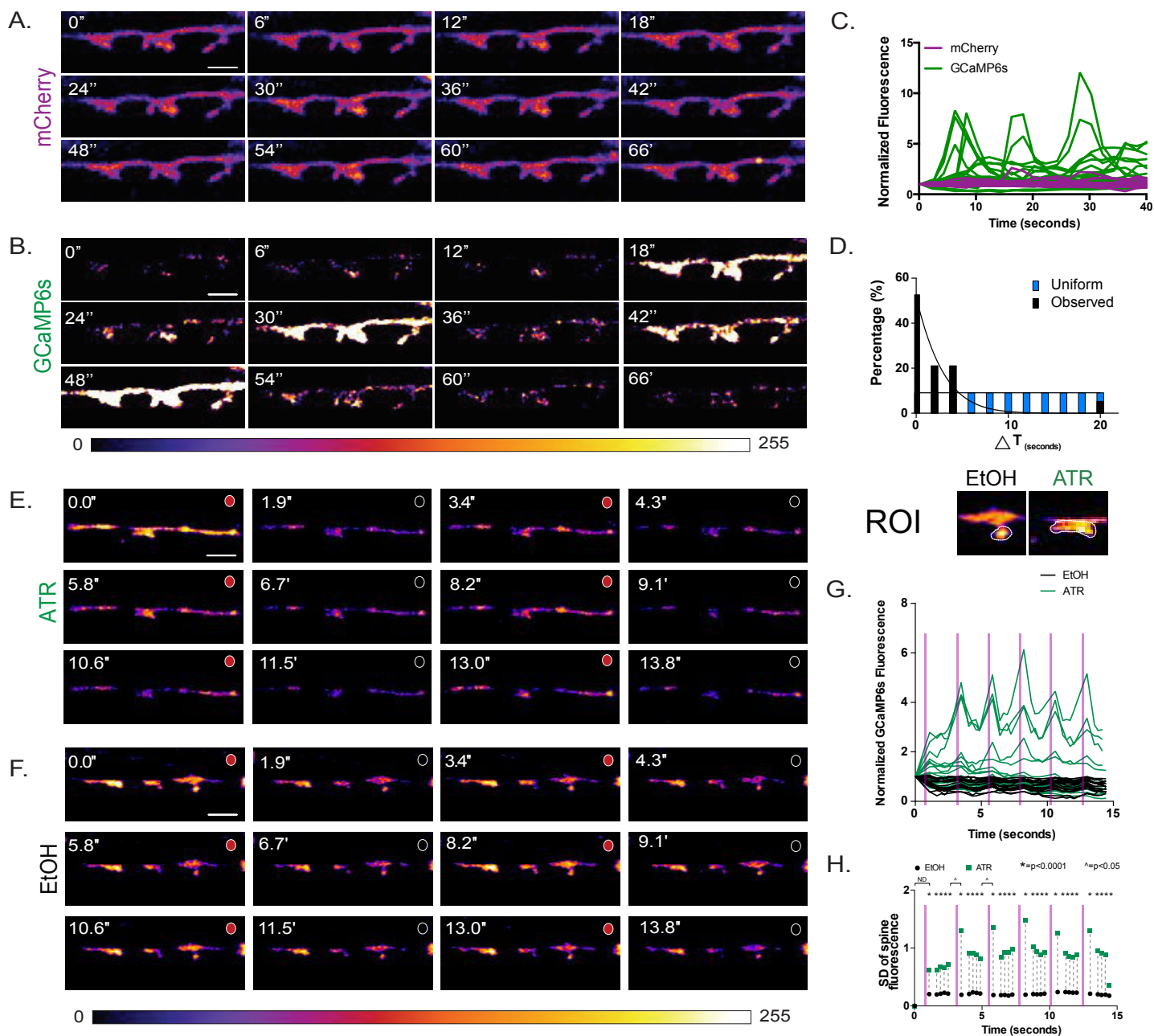


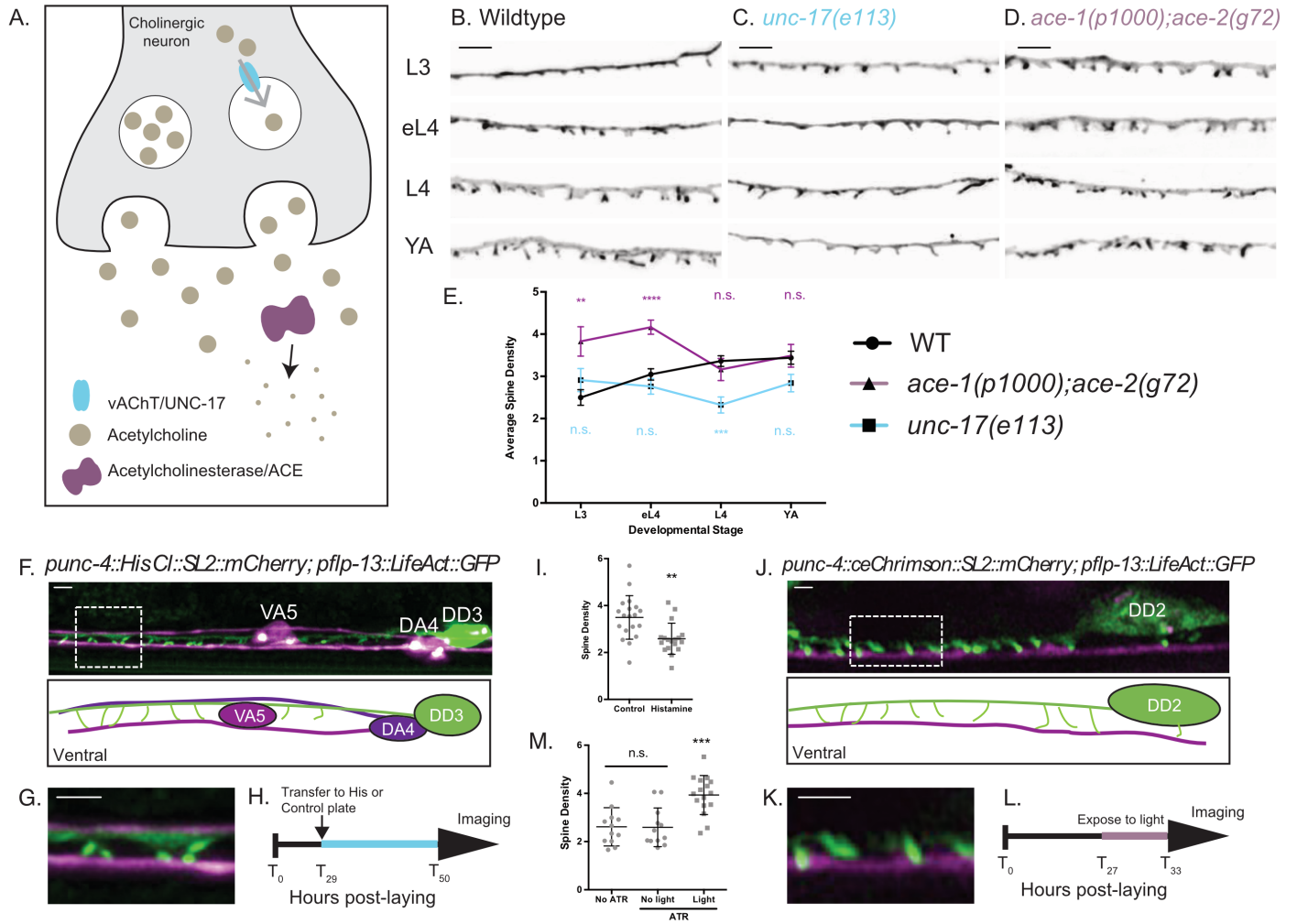
C.

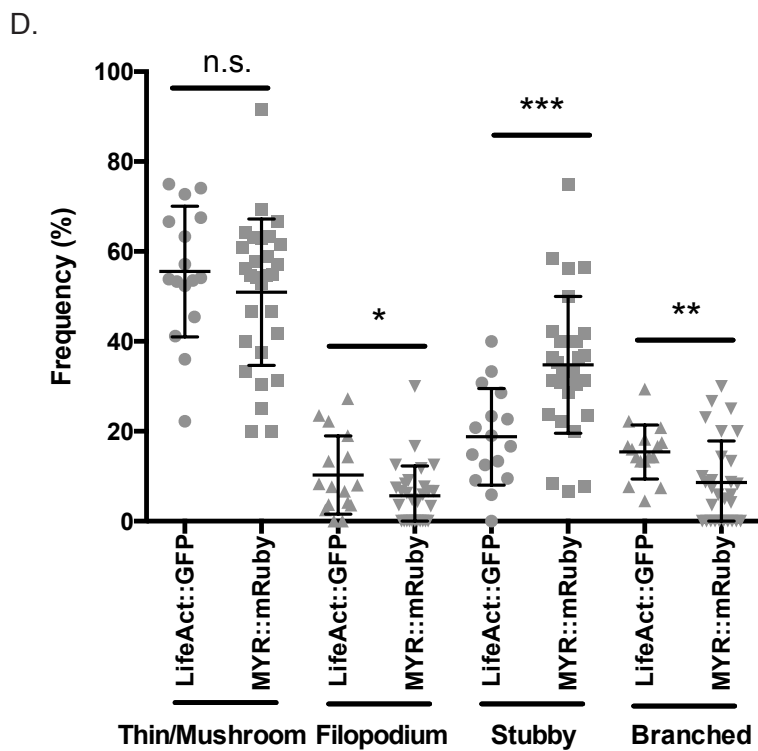
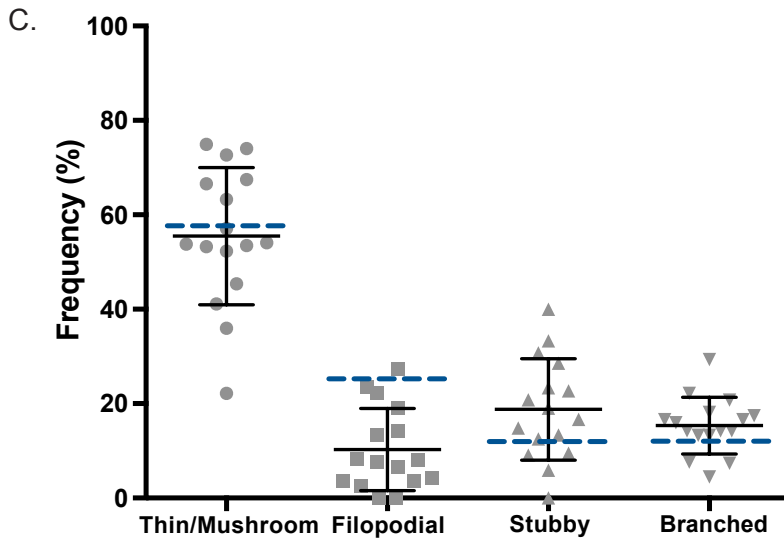
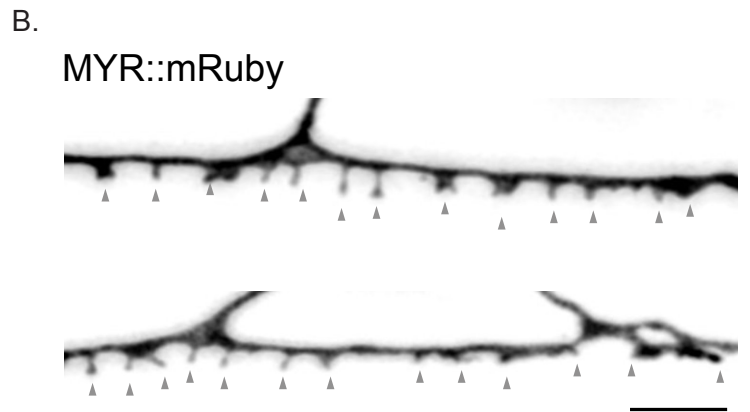
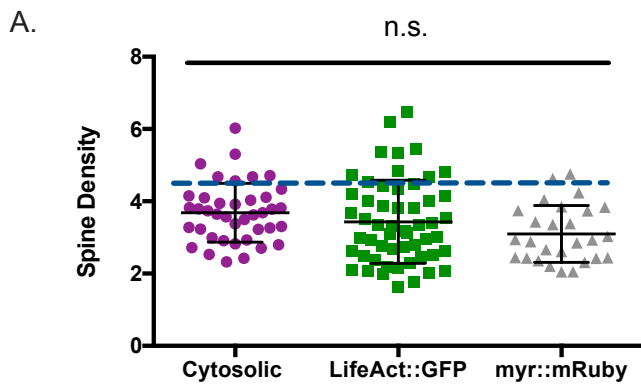


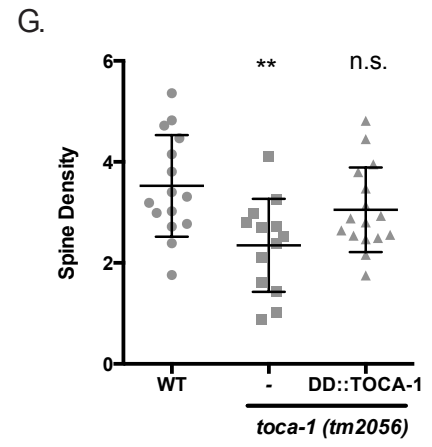
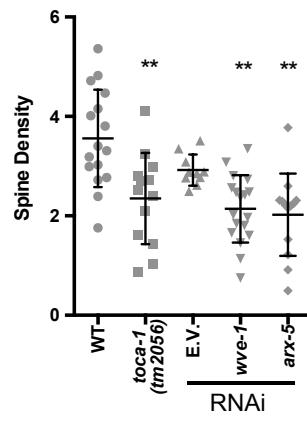
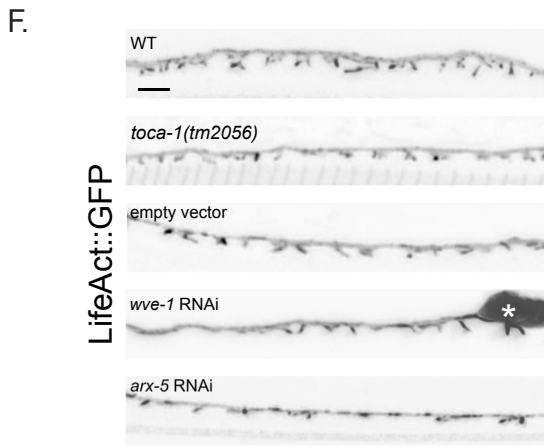
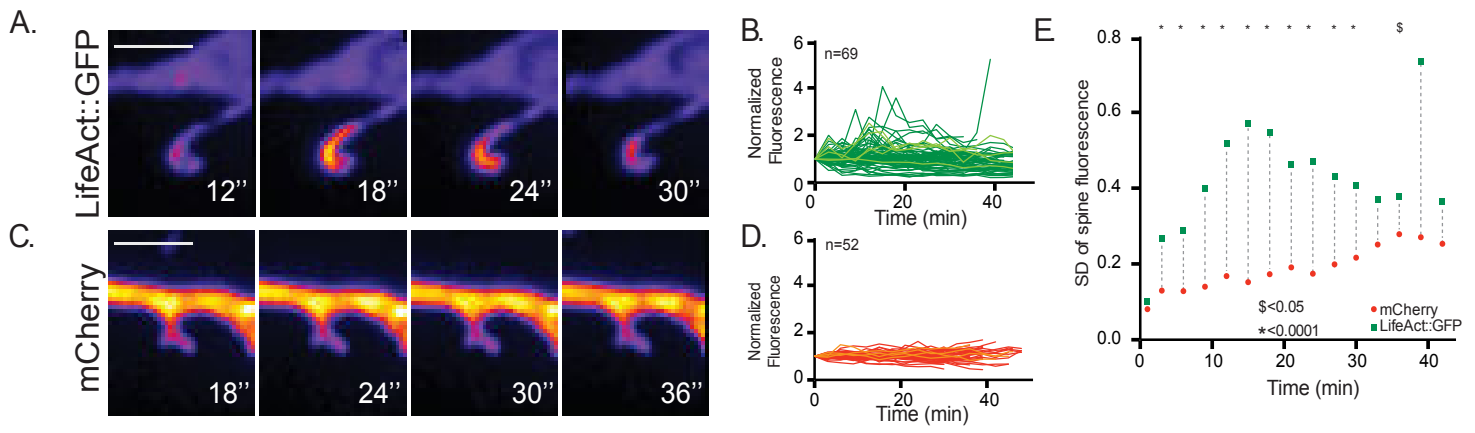
D. Mitochondria in DD postsynaptic dendrite



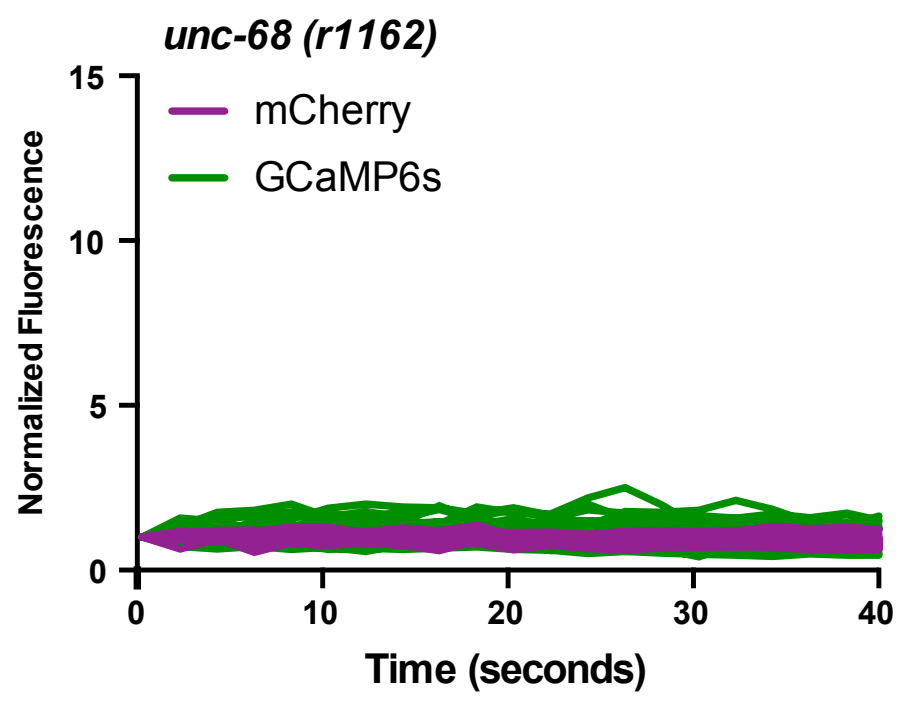




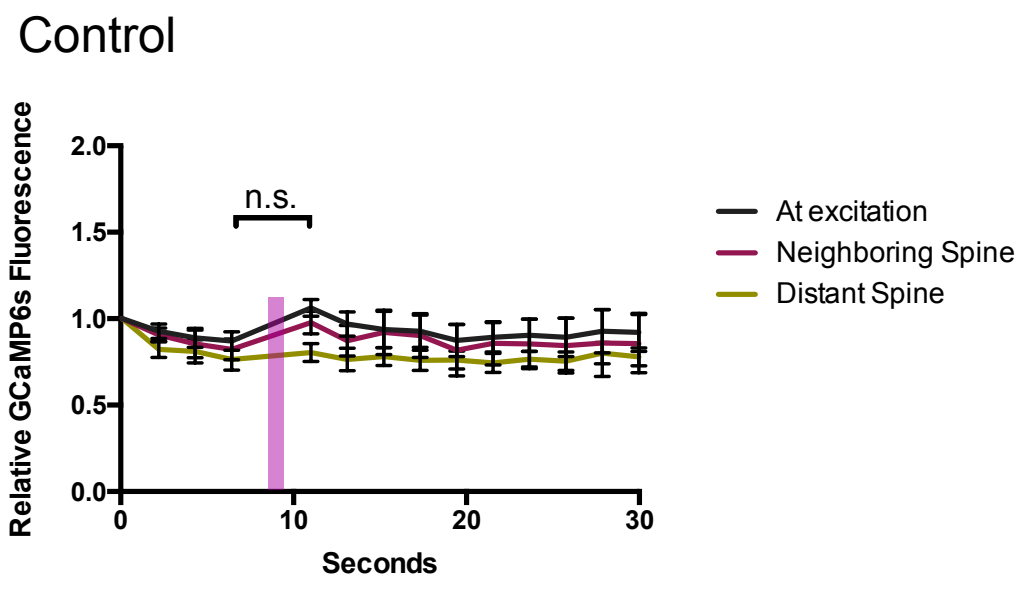




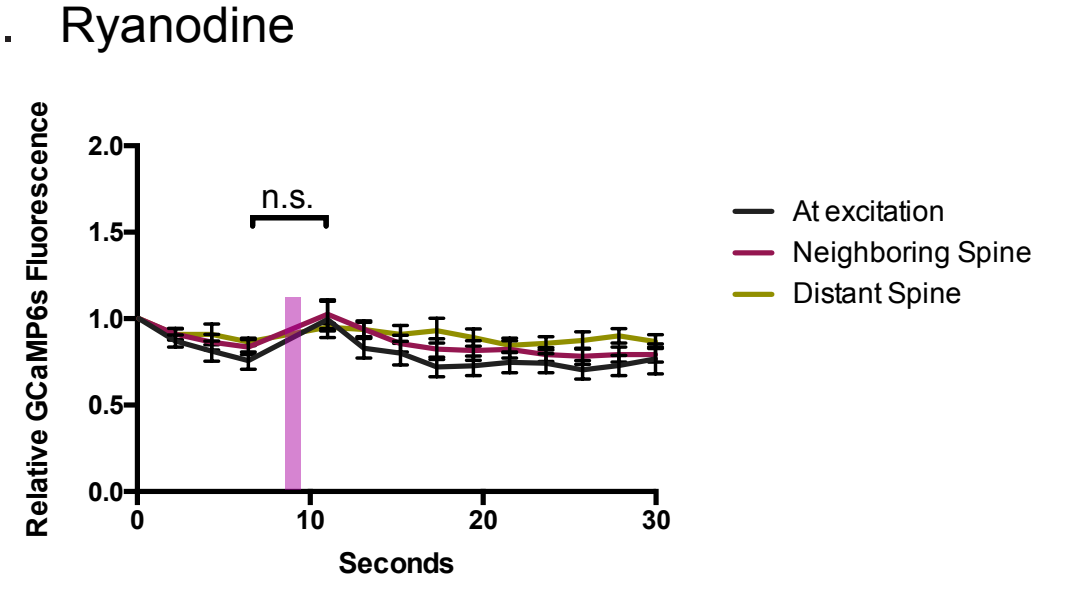
A.

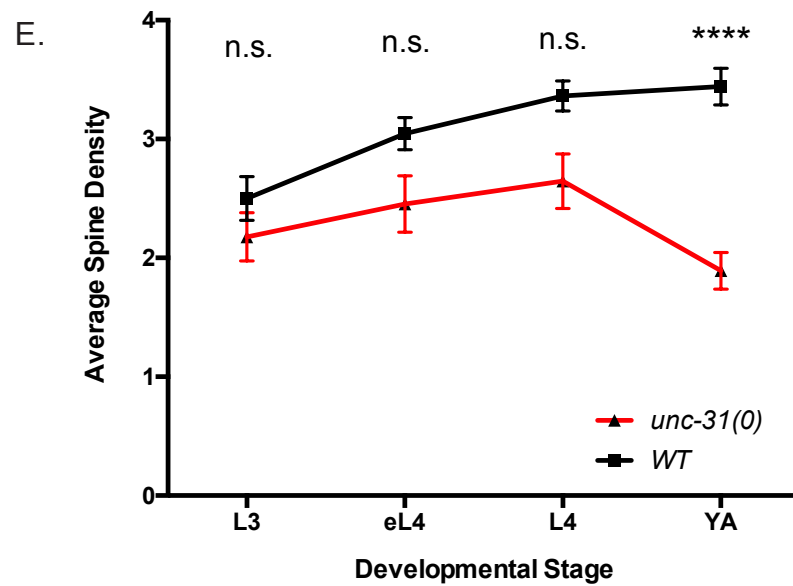
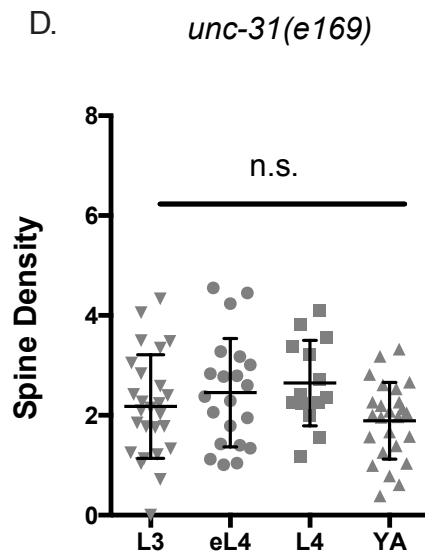
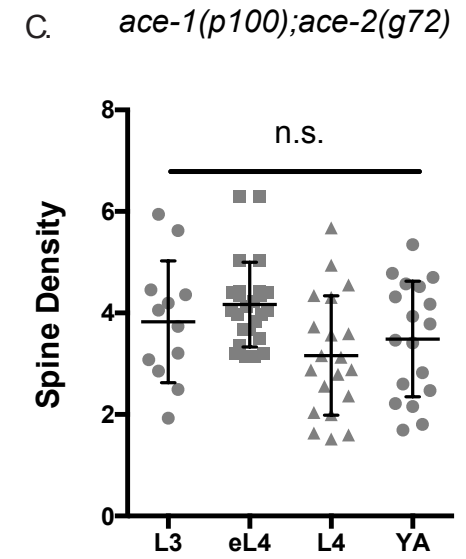
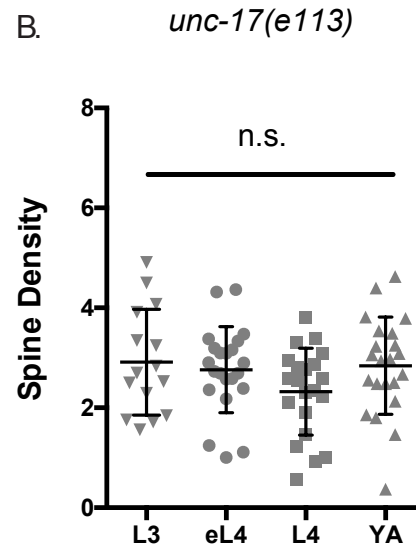
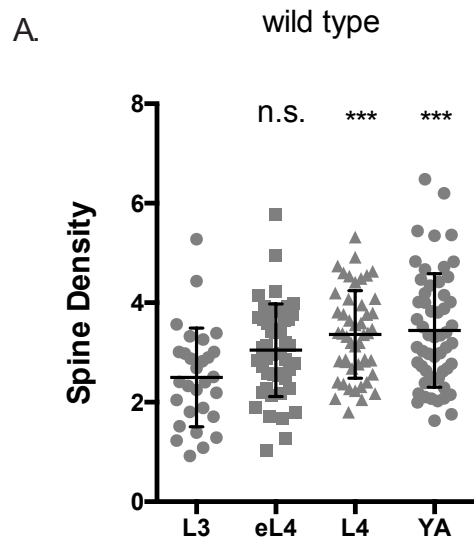


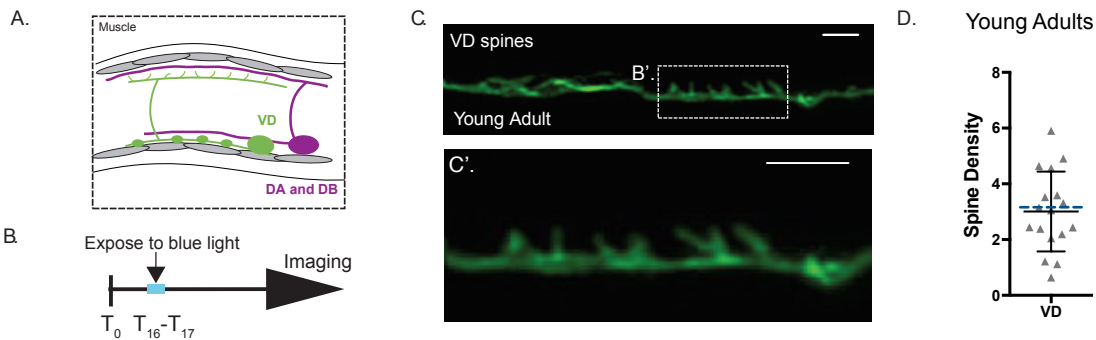
B.



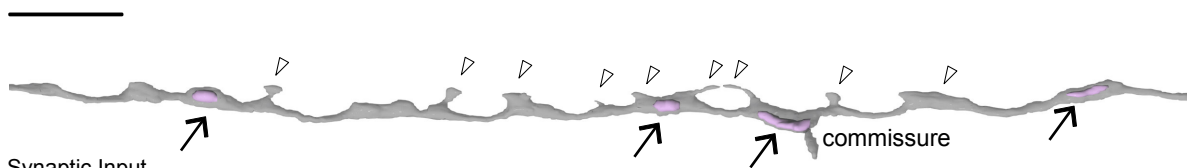
C.







E. Mitochondria in VD neurons



F. Synaptic Input

